# System Identification for a Subscale Tiltrotor eVTOL Aircraft from Hover Flight-Test Data

Benjamin M. Simmons[*] and Kasey A. Ackerman[†]
*NASA Langley Research Center, Hampton, Virginia 23681*

**This paper describes the system identification process and hover flight-test modeling results for a subscale tiltrotor electric vertical takeoff and landing (eVTOL) vehicle built at NASA Langley Research Center. The vehicle, referred to as the Research Aircraft for eVTOL Enabling techNologies (RAVEN) Subscale Wind-Tunnel and Flight Test (SWFT) model, operates as a dynamic modeling and flight controls research testbed used to advance eVTOL aircraft technology. Expanding on previous eVTOL aircraft system identification research leveraging wind-tunnel testing and flight simulations, a modeling approach using flight data is presented for the RAVEN-SWFT aircraft. The full system identification methodology is outlined, including the experiment design, flight testing, and model identification steps. An overview of the current flight-test envelope expansion status is included, alongside modeling results obtained from hover flight testing using two types of maneuvers employing multisine excitation inputs. The flight-derived model is shown to have a close model fit and good prediction performance in the hover flight regime. The methods discussed in the paper help to inform efficient flight-test-based modeling strategies for many current and future eVTOL aircraft.**

## Nomenclature

$a_x, a_y, a_z$ = body-axis translational acceleration, ft/s$^2$
$g$ = gravitational acceleration, ft/s$^2$
$I_x, I_y, I_z, I_{xz}$ = aircraft inertia tensor elements, slug·ft$^2$
$h_x, h_y, h_z$ = net body-axis propulsion system angular momentum components, slug·ft$^2$/s
$L, M, N$ = body-axis aero-propulsive rolling, pitching, and yawing moment, ft·lbf
$m$ = aircraft mass, slug
$n_1, n_2, \ldots, n_6$ = proprotor rotational speeds, rev/s
$p, q, r$ = body-axis angular velocity components, rad/s or deg/s
$u, v, w$ = body-axis translational velocity components, ft/s
$X, Y, Z$ = body-axis aero-propulsive forces, lbf
$\delta_{c_1}, \delta_{c_2}, \ldots, \delta_{c_6}$ = proprotor collective pitch angles, rad or deg
$\delta_{f_1}, \delta_{f_2}, \ldots, \delta_{f_6}$ = flaperon deflection angles, rad or deg
$\delta_{t_1}, \delta_{t_2}, \delta_{t_3}, \delta_{t_4}$ = nacelle tilt angles, rad or deg
$\delta_r$ = rudder deflection angle, rad or deg
$\delta_s$ = stabilator deflection angle, rad or deg
$\phi, \theta, \psi$ = Euler roll, pitch, and yaw angles, rad or deg

*Superscripts*
$^T$ = transpose
$^{-1}$ = matrix inverse
$\hat{}$ = estimate
$\dot{}$ = time derivative
$\tilde{}$ = Fourier transform
$^\dagger$ = complex conjugate transpose

---

[*] Research Aerospace Engineer, Flight Dynamics Branch, Member AIAA.

[†] Research Aerospace Engineer, Dynamic Systems and Control Branch, Member AIAA.

# I. Introduction

Aviation technology advances for hybrid and electric distributed propulsion systems have enabled development of new vehicle configurations for Advanced Air Mobility (AAM) applications. Urban Air Mobility (UAM), a critical subset of AAM, requires vehicles capable of vertical takeoff and landing, precise low-speed maneuverability to operate in congested areas, and seamless conversion to more efficient cruise flight. Electric vertical takeoff and landing (eVTOL) vehicles are currently seen as encouraging candidates to fulfill UAM missions. Various eVTOL designs are currently being examined, including tiltwing, tiltrotor, and lift+cruise configurations [1–6]. These vehicles generally combine elements from traditional rotary-wing and fixed-wing aircraft, as well as modern distributed propulsion systems, vastly expanding the aircraft design space. As of November 2025, over 1150 eVTOL aircraft concepts have been cataloged by the Vertical Flight Society [6], highlighting the design space flexibility and investments in this emerging aircraft type.

Although there is currently a promising outlook for the broad use of eVTOL aircraft, numerous critical research areas—such as flight control system development, air traffic management, handling qualities, fault tolerance, and autonomy—need to be examined further before eVTOL vehicles can be integrated into the national airspace system. A multidisciplinary enabling research need in these areas is a flight dynamics simulation that includes high-fidelity aero-propulsive models. The efficient development of accurate aero-propulsive models, however, is complicated by several common eVTOL vehicle features, including: a large number of propulsors and control surfaces, significant aero-propulsive coupling, unstable vehicle dynamics, and substantial aerodynamic variability throughout a wide range of operational flight conditions.

The primary objective of aero-propulsive modeling for a flight vehicle is to accurately characterize the applied aerodynamic forces and moments in flight, which drive flight dynamic behavior. Therefore, using flight data for aerodynamic characterization typically yields the most accurate representation of the aircraft to predict actual flight motion. Empirical mathematical modeling of flight mechanics using input and output data measured from an aircraft is referred to as aircraft system identification [7–9]. Generally, aircraft system identification encompasses the steps needed to determine mathematical expressions describing the applied forces and moments as a function of state and control variables, using data collected in dedicated experiments. Although system identification techniques are well established for standard fixed-wing and rotary-wing aircraft modeling applications [10–15], eVTOL aircraft system identification requires further study to address unique configuration challenges that complicate efficient and accurate aero-propulsive model development. Formulation of an approach for eVTOL aircraft system identification from flight data and demonstration of the techniques using hover flight data acquired from a complex subscale tiltrotor vehicle constitute the main topics of this paper.

The paper is organized as follows: Section II introduces the experimental aircraft and Sec. III provides pertinent background information on related system identification research. Section IV presents the system identification approach. The current flight-test status is described in Sec. V and hover modeling results are given in Sec. VI. Overall conclusions are summarized in Sec. VII.

# II. Aircraft

To help advance eVTOL aircraft research, NASA Langley Research Center has built the Research Aircraft for eVTOL Enabling techNologies (RAVEN) Subscale Wind-Tunnel and Flight Test (SWFT) model [16]. The RAVEN-SWFT is a 28.6% scale version of the RAVEN 1000-lb class eVTOL aircraft concept [17], which was designed in a collaborative effort between NASA Langley and the Georgia Institute of Technology. The RAVEN aircraft is a tiltrotor eVTOL configuration with six variable-pitch proprotors. The front four proprotors tilt forward and are operational throughout the entire flight envelope. The rear two proprotors do not tilt and serve as lifting proprotors in hover and transition. The aircraft control surfaces include six flaperons, a stabilator, and a rudder. In total, the vehicle has 24 independent control effectors:

- Six proprotor rotational speeds ($n_1, n_2, \ldots, n_6$)
- Six proprotor collective pitch angles ($\delta_{c_1}$, $\delta_{c_2}$, . . . , $\delta_{c_6}$)
- Four nacelle tilt angles ($\delta_{t_1}$, $\delta_{t_2}$, $\delta_{t_3}$, $\delta_{t_4}$)
- Six flaperon deflection angles ($\delta_{f_1}$, $\delta_{f_2}$, . . . , $\delta_{f_6}$)
- One stabilator deflection angle ($\delta_s$)
- One rudder deflection angle ($\delta_r$)

The propulsor and control surface definitions are included on a schematic of the RAVEN aircraft shown in Fig. 1. Flaperon and stabilator deflections are defined as positive trailing edge down. Rudder deflection is defined as positive trailing edge left. Nacelle tilt angle settings of 0 deg correspond to the horizontal, forward flight position; nacelle tilt angle settings of 90 deg correspond to the vertical position used near hover. Proprotors 1, 3, and 5 rotate counterclockwise and proprotors 2, 4, and 6 rotate clockwise, as viewed from the perspective of each electric motor located behind its respective proprotor.

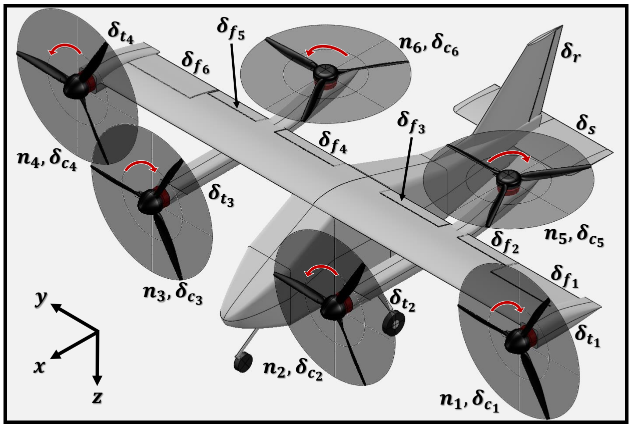

**Fig. 1 RAVEN control effector definitions.**

**Table 1 RAVEN-SWFT properties**

| Property | Value | Units |
|---|---|---|
| mass, $m$ | 1.185 | slug |
| roll moment of inertia, $I_x$ | 2.169 | slug·ft$^2$ |
| pitch moment of inertia, $I_y$ | 0.897 | slug·ft$^2$ |
| yaw moment of inertia, $I_z$ | 2.551 | slug·ft$^2$ |
| product of inertia, $I_{xz}$ | 0.0046 | slug·ft$^2$ |
| mean aerodynamic chord, $\bar{c}$ | 0.760 | ft |
| wingspan (excluding nacelles), $b$ | 5.71 | ft |
| wing reference area, $S$ | 4.34 | ft$^2$ |
| proprotor diameter, $D$ | 1.625 | ft |

The RAVEN-SWFT, pictured in Fig. 2, was designed as a flight dynamics and controls research testbed that can be used in both wind-tunnel and flight-test studies [16]. The aircraft inertial and geometric properties are listed in Table 1. The inertia tensor elements are assumed to be constant across the flight envelope, which is justified because the experimentally determined diagonal elements of the hover and forward flight inertia tensor [16] differ by less than 1%.

**(a) Front view (cruise configuration)** **(b) Overhead view (hover configuration)**

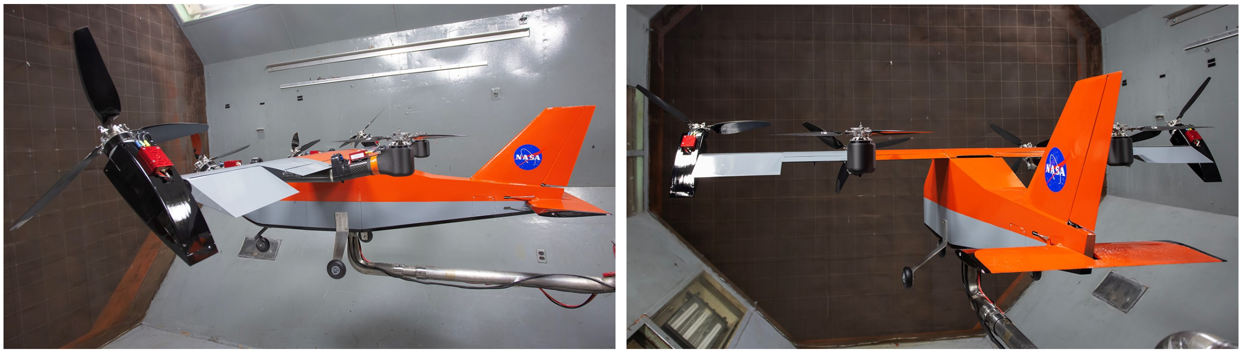

**(c) Side view (mid-transition configuration)** **(d) Rear view (mid-transition configuration)**

**Fig. 2 RAVEN-SWFT mounted in the NASA Langley 12-Foot Low-Speed Tunnel. (Credit: NASA)**

The RAVEN-SWFT is NASA Langley's newest and most capable subscale eVTOL research aircraft. Two predecessor subscale eVTOL vehicles were the GL-10 tiltwing tilt-tail aircraft [18] and LA-8 tandem tiltwing aircraft [19, 20]. The

GL-10 and LA-8 both had successful wind-tunnel and flight-test campaigns that yielded many eVTOL aircraft research advances [21–29], but were discontinued before testing custom transition flight control software and flight-test system identification methods requiring automated input injection capabilities. The RAVEN-SWFT aircraft was engineered to continue eVTOL aircraft research efforts initiated on the GL-10 and LA-8, with a major emphasis on creating a flight-test asset for advanced dynamic modeling and flight controls research. Accordingly, being able to expeditiously design, integrate, test, and refine custom flight control algorithms was an essential aspect of vehicle development. Reference [30] discusses the RAVEN-SWFT modeling and control software development approach applied through completed wind-tunnel testing and initial flight testing.

The flight control algorithm, discussed further in Ref. [30], was developed with a model-based design approach using the RAVEN-SWFT flight dynamics simulation. The overall RAVEN-SWFT flight control algorithm is composed of a nested-loop architecture, shown in Fig. 3, including an attitude-control inner loop and a velocity-control outer loop. The design approach includes a linear quadratic integral (LQI) [31] model-following control framework with a static feedforward element. A weighted pseudo-inverse control allocation approach is employed to appropriately distribute the control effector commands. Figure 4 shows the general structure of the inner- and outer-loop control laws. Notably, because the authors have full authority to modify the RAVEN-SWFT flight control software, integration of the automated programmed test input (PTI) injection capability discussed later in the paper is straightforward and readily accessible.

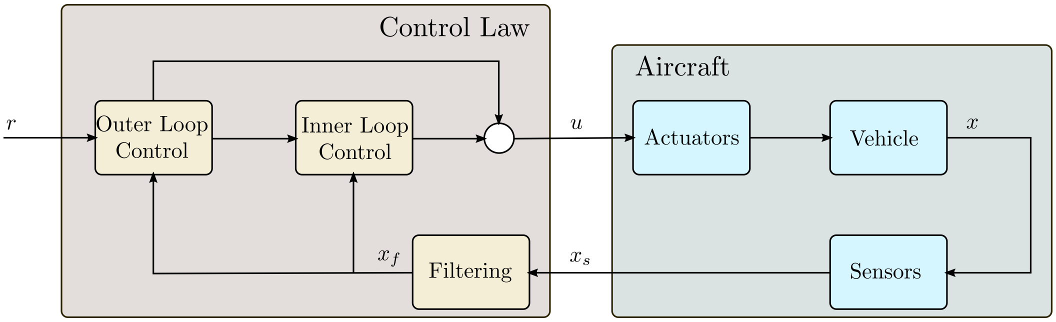

**Fig. 3 Schematic of the overall RAVEN-SWFT flight control algorithm.**

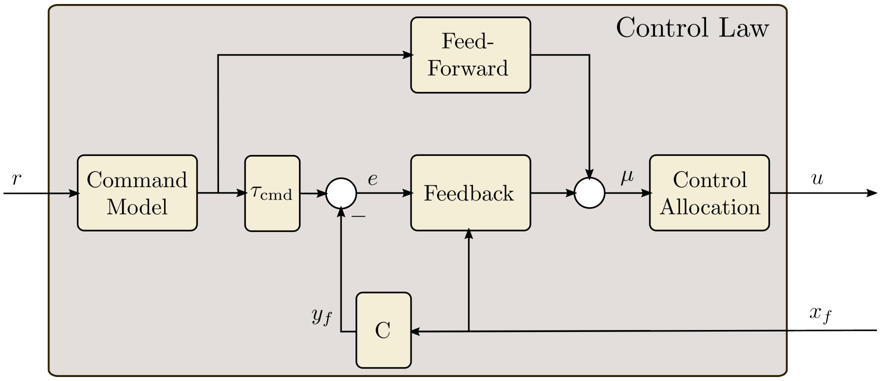

**Fig. 4 Schematic of the inner- and outer-loop control law structure.**

As described with greater detail in Ref. [30], the RAVEN-SWFT flight software is implemented on a Pixhawk® flight computer running PX4 [32]. The flight control system, created using MATLAB®/Simulink®, is deployed onto the Pixhawk using the MathWorks® UAV Toolbox and its Support Package for PX4 Autopilots [33]. The custom RAVEN-SWFT flight control algorithm replaces the default PX4 control laws, while retaining most of the other functions within the PX4 Autopilot firmware. The Pixhawk onboard RAVEN-SWFT interfaces with an external inertial navigation system (INS) that provides improved state estimates and sensor measurements. The flight computer records inertial

---

The use of trademarks or names of manufacturers in this report is for accurate reporting and does not constitute an official endorsement, either expressed or implied, of such products or manufacturers by the National Aeronautics and Space Administration.

measurement unit (IMU), INS, airspeed, and internal controller data. An additional RAVEN-SWFT data acquisition system (DAS) logs signals from the electronic speed controllers (ESCs), control surface servo-actuators, and an air-data probe. All data used for system identification are logged at a 50 Hz or greater sample rate.

# III. Background

Recent system identification studies addressing challenges similar to those seen by eVTOL vehicles are briefly noted to provide background for the present research. In Ref. [34], an approach is formulated to efficiently estimate the effectiveness of 16 different control surfaces on a generic commercial transport aircraft. During a single flight maneuver, orthogonal phase-optimized multisine signals were simultaneously applied to each control surface allowing for each control derivative to be independently characterized. The X-56 aeroelastic technology demonstrator aircraft, which has 10 control surfaces and two engines, implemented a similar excitation strategy for system identification [35–37]. Control effectors were excited independently and in pairs using sets of different multisine signals enabling efficient model identification [38]. A system identification effort for a fixed-wing vehicle with eight distributed electric ducted fans (EDFs) is described in Ref. [39]. The control surfaces were actuated using multisine signals and throttle doublets were applied to individual EDFs to collect data used for modeling. Modeling of multirotor vehicles from flight data using various input types and modeling approaches has received significant focus and has been documented in numerous publications [40–51]. In Refs. [52–54], multisine signals were applied to each propulsor on multirotor vehicles to facilitate estimation of dynamic models. References [55, 56] describe recent system identification efforts pursued for lift+cruise eVTOL aircraft using doublet and frequency sweep inputs. Hover system identification findings for an industry prototype vectored-thrust eVTOL aircraft configuration that exercised multisine inputs on propulsors and control surfaces are reported in Ref. [57].

The modeling techniques discussed in this paper expand on previous aero-propulsive modeling, system identification, and wind-tunnel testing research conducted using the NASA LA-8 and RAVEN-SWFT vehicles. Reference [28] describes the process applied to develop an aero-propulsive model for the LA-8 aircraft using static powered-airframe wind-tunnel testing. Because eVTOL vehicles have aerodynamic features of both rotary-wing and fixed-wing aircraft, as well as complicated vehicle-specific attributes, traditional aircraft aerodynamic modeling strategies must be adapted to effectively characterize eVTOL aircraft. Accordingly, postulation of aero-propulsive modeling strategies tailored to eVTOL aircraft using experimental data was a major focus; this included formulating explanatory and response variables used for modeling, designing experiments to enable accurate and efficient characterization of important aerodynamic phenomena, developing approaches to accurately describe aerodynamics over the full transition flight envelope, and investigating the propulsion-airframe interactions that are ubiquitous in eVTOL vehicles. The LA-8 aero-propulsive model delivered from this work was composed of a collection of nonlinear response surface equations predicting the aero-propulsive forces and moments applied to the vehicle at several airspeed conditions throughout the flight envelope. A similar static wind-tunnel testing approach was applied to the RAVEN-SWFT aircraft in Ref. [58] with multiple experiment design and test execution improvements. As an extension of this wind-tunnel testing research, Ref. [29] demonstrated an alternative modeling method for the LA-8 aircraft employing multisine signals on control surfaces and propulsors to substantially increase static wind-tunnel testing efficiency.

Based on the insights obtained from LA-8 wind-tunnel studies and established aircraft system identification methods [7–9], Ref. [59] proposed and demonstrated a generalized flight-based system identification approach for eVTOL aircraft using the LA-8 flight dynamics simulation. Starting from trimmed flight at different parts of the operational envelope, multisine inputs were applied to each propulsor and control surface facilitating acquisition of information-rich simulated flight data enabling accurate model identification. The findings from this work were aimed at informing future eVTOL aircraft flight-based system identification efforts; thus, an obvious extension is to verify the approach with real data collected in flight testing for an eVTOL aircraft. In a complementary experimental study for RAVEN-SWFT, an analogous method was implemented in a free-motion three degree-of-freedom (3DOF) wind-tunnel test, providing initial empirical validation of the approach for modeling the aero-propulsive moments [60].

The present work expands previous efforts by refining and demonstrating efficient system identification techniques for eVTOL aircraft using data obtained in RAVEN-SWFT flight testing. Although there have been multiple related publications by the authors, as outlined above, this paper will be the first to include RAVEN-SWFT flight-test system identification results and the associated findings from ongoing flight testing.

# IV. System Identification Approach

Aircraft system identification using flight data typically follows the process summarized in Fig. 5. Applications requiring an accurate dynamic model, such as control law development or validation of aerodynamic predictions derived from computational methods and/or ground testing, often motivate undertaking flight-test system identification efforts. Overall objectives for the identified model are established by the desired accuracy and range of validity needed for the target application. Flight testing is then planned and executed to perturb the aircraft dynamic response over the areas of desired model applicability. Next, data processing procedures are applied to evaluate flight data quality and prepare the data for model identification. Based on the acquired data and insight into the flight physics, a suitable model structure is subsequently formed and the unknown parameters within the model are estimated. Validation steps follow identification of the model to assess its accuracy and prediction performance, allowing for determination of the model adequacy for its intended purpose. In a case where the model is designated to be inadequate, corrective steps are implemented to conduct further testing and/or analysis procedures to improve the model adequacy. Once the model is deemed to be adequate, it can then be used for its desired application. Additional information on each part of the system identification process, as applied for the RAVEN-SWFT aircraft, is provided in the following subsections. Although the results presented in this paper focus on the hover flight regime, the general approach discussed in this section pertains to system identification throughout the flight envelope. The experiment design and model identification methods applied in this work were adapted from the System IDentification Programs for AirCraft (SIDPAC) software toolbox [7, 61].

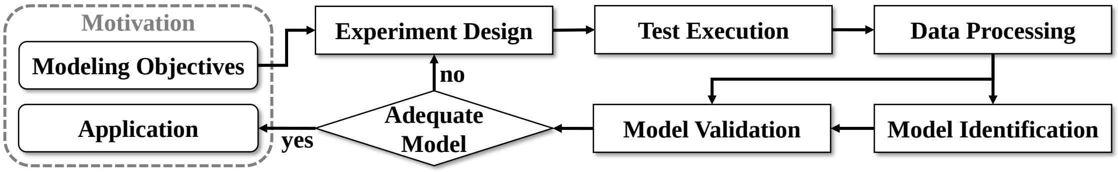

**Fig. 5 General flight-test system identification process.**

## A. Motivation

The system identification study described in this paper had multiple objectives. First, from a research perspective, the modeling results were desired to experimentally validate and refine a general approach for flight-test system identification of eVTOL aircraft. Second, from the perspective of RAVEN-SWFT envelope expansion and flight control system development, the flight-derived modeling results are needed to develop a high-fidelity aero-propulsive model in the high-speed portion of the RAVEN-SWFT flight envelope. As discussed further in Refs. [58, 60], static and dynamic powered-airframe wind-tunnel tests conducted in the NASA Langley 12-Foot LST were used to develop a transition aero-propulsive model for RAVEN-SWFT up to a dynamic pressure setting of $\bar{q} = 5$ lbf/ft$^2$ (a freestream airspeed of $V = 65$ ft/s at standard sea level conditions)—the practical limit for testing eVTOL vehicles in the facility. For RAVEN-SWFT, the powered-airframe wind-tunnel testing covered just over 50% of the transition envelope. At $\bar{q} = 5$ lbf/ft$^2$ and below, the current RAVEN-SWFT aero-propulsive model is high-fidelity and is not expected to require much, if any, adjustment using flight data. Above $\bar{q} = 5$ lbf/ft$^2$, preliminary low-fidelity estimates of the vehicle aero-propulsive forces and moments were made to create an initial full envelope model; however, model identification from flight data is expected to be required to produce a more accurate aero-propulsive model in the high-speed portion of the RAVEN-SWFT flight envelope. The updated flight-derived high-speed aero-propulsive model is planned to be integrated into the flight dynamics simulation and be used to update parameters in the flight control algorithm.

## B. Experiment Design

Specific aircraft system identification flight maneuvers are designed to excite aircraft dynamic motion and facilitate acquisition of informative flight data used for modeling. An important capability of the custom RAVEN-SWFT flight control system is a PTI injection capability used to conduct system identification flight testing. As demonstrated in Fig. 6, the PTI excitations are added to the reference command and control effector signals, before and after the flight control laws, respectively. The automatic inputs programmed into the RAVEN-SWFT flight control system included multistep [7, 8], frequency sweep [7, 9], and multisine excitations [7].

Multistep square wave inputs [e.g., doublet (1-1), 1-2-1, and 3-2-1-1 inputs] and frequency sweep inputs are summed into the reference command PTI excitations upstream of the control laws. Currently, doublet commands are used

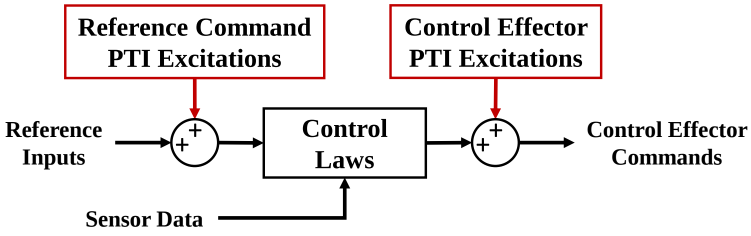

**Fig. 6 PTI injections relative to the control laws.**

to evaluate the tracking performance of the flight controller and can also serve as system identification validation maneuvers. The more complex multistep and frequency sweep inputs have been executed for software verification purposes, but are not currently planned for use in RAVEN-SWFT flight testing. Given the large number of control effectors and extensive aero-propulsive complexity present for eVTOL vehicles, multisine inputs are the preferred input type for efficient open-loop model identification.

Orthogonal phase-optimized multisine inputs [7, 62–64] have been used as the primary system identification PTI type for the RAVEN-SWFT aircraft. A multisine input is composed of a sum of multiple sinusoidal functions with different amplitudes, frequencies, and phase angles. For $m$ total control effectors, the $j$th input signal $u_j(t)$ is defined as

$$u_j(t) = \sum_{k \in K_j} A_j \sqrt{P_k} \sin\left(\frac{2\pi k t}{T} + \phi_k\right), \qquad j = 1, 2, \dots, m \tag{1}$$

where $A_j$ is the signal amplitude, $P_k$ is the $k$th power fraction (with $\sum_{k \in K_j} P_k = 1$), $\phi_k$ is the $k$th phase angle defined on the interval $(-\pi, +\pi]$, and $t$ is the elapsed time. The available frequencies are $f_k = k/T,\ k = 1, 2, \dots, K$, where $T$ is the fundamental period and $K/T$ is the highest excitation frequency. The frequency components are chosen to cover the frequency range of the relevant system dynamics, with each control effector assigned unique frequencies to make all inputs orthogonal in both the time domain and frequency domain. The phase angles are optimized to obtain a minimum relative peak factor, which serves to keep the aircraft near its nominal operating point while still delivering the same input energy as the unoptimized signal. Furthermore, by concurrently moving all control effectors in an independent manner and simultaneously exciting all vehicle dynamics of interest, use of multisine inputs results in highly informative and streamlined flight testing. Data from a single well-designed multisine maneuver is typically sufficient to identify a comprehensive aircraft aero-propulsive model around a reference flight condition, with flexibility to include nonlinear aerodynamic phenomena and control interactions.

As first outlined in Ref. [30], for RAVEN-SWFT flight testing, unique multisine signals were generated for each of the 24 independent control effectors. Additionally, multisine signals were designed for the reference commands $\eta_{\text{lon}}$, $\eta_{\text{lat}}$, $\eta_{\text{dir}}$, and $\eta_{\text{ver}}$ tracked by the control system to provide additional state perturbations, elevating the magnitude of certain state disturbances resulting from control effector PTI injections. In and near hover, $\eta_{\text{lon}}$ is a forward velocity command, $\eta_{\text{lat}}$ is a side velocity command, $\eta_{\text{dir}}$ is a yaw rate command, and $\eta_{\text{ver}}$ is a vertical velocity command. Directional reference command multisine inputs were observed to be particularly useful for accurate estimation of lateral speed $v$ and yaw rate $r$ related parameters in RAVEN-SWFT 3DOF wind-tunnel testing [60]. Also, system identification flight testing for a vectored-thrust eVTOL aircraft revealed that supplementing multisine control effector inputs with additional reference command inputs improved hover state derivative identification accuracy [57]. Between the control effector and reference command multisine signals, there are 28 total independent excitation signals that can be applied simultaneously.

The RAVEN-SWFT flight-test multisine inputs were constructed by distributing several unique harmonic components to each multisine signal, where the overall frequency range was defined to be between 0.05 Hz and 1.75 Hz to encompass the frequencies where the rigid-body dynamics were expected to manifest. For the reference commands and slower moving control effectors, the harmonic components were limited to remain within the approximate bandwidth of each signal. Multisine signals for the collective pitch, outboard tilt, stabilator, flaperon, and rudder spanned full frequency range and each included 18 frequency components. For the proprotor rotational speed, inboard tilt, and reference commands, multisine harmonic components were concentrated into lower frequencies in accordance with their lower bandwidth and contained 16, 12, and 5 components, respectively. The frequency components for each signal were allocated in an alternating manner and were spread to prevent nearby control effectors from having neighboring frequency components, similar to the philosophy used in Ref. [38].

Figure 7 shows the input spectra for the RAVEN-SWFT flight-test multisine signals, which includes 428 total harmonic components. The frequency components are between $f_{\min} = 0.05$ Hz and $f_{\max} = 1.754$ Hz. The multisine fundamental period is $T = 260$ seconds and, thus, the frequency resolution is $\Delta f = 1/T = 0.00385$ Hz. The first 20 seconds of each multisine signal with $A_j = 1$ is displayed in Fig. 8. For multisine maneuvers executed in RAVEN-SWFT flight testing, the target maneuver length is 60 seconds. As discussed and demonstrated in Refs. [29, 59], there are practical advantages to having a multisine fundamental period longer than the target maneuver length for eVTOL aircraft, even though some minor correlation among the designed input signals is introduced when this is the case.

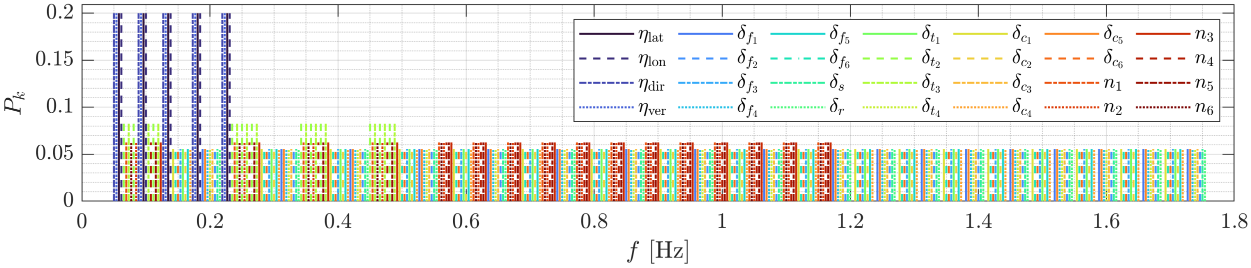

**Fig. 7 RAVEN-SWFT flight-test multisine input spectra for each reference command and control effector.**

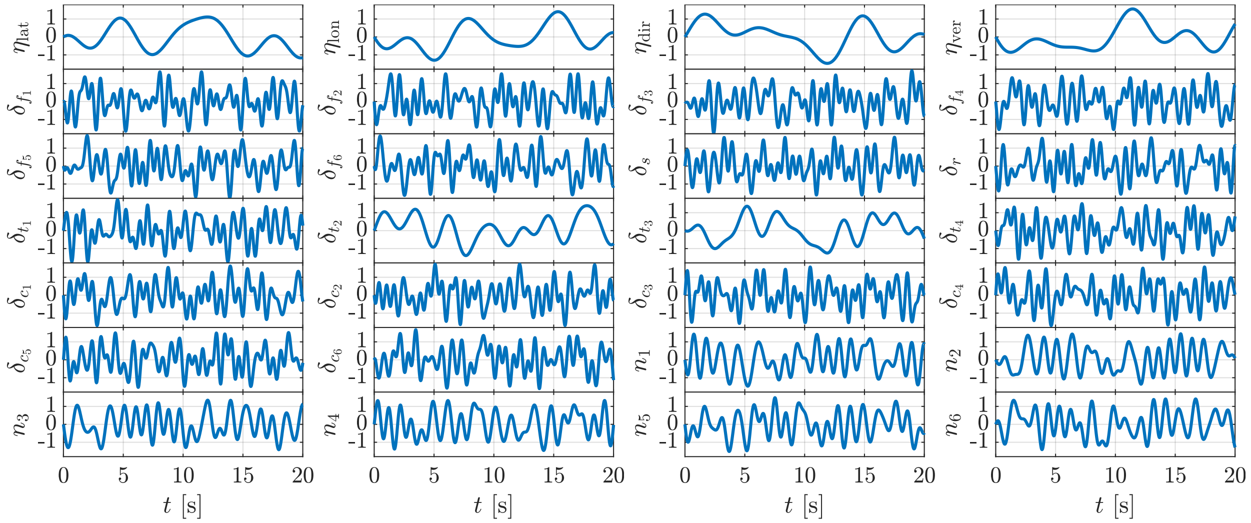

**Fig. 8 Normalized RAVEN-SWFT multisine input signal for each reference command and control effector.**

The RAVEN-SWFT vehicle dynamics are unstable over a significant portion of its operational flight conditions, requiring the feedback control system to always be active when operating the aircraft. Consequently, the original multisine signals shown in Fig. 8 are distorted and become somewhat correlated during flight testing. Therefore, the modeling accuracy may be slightly degraded compared to the modeling results for a vehicle that does not require a control system to be operating during system identification maneuvers. Nonetheless, despite the signal waveform distortion and diminished orthogonality, the signals used for modeling still generally remain sufficiently decorrelated for successful model identification as a result of the control effector excitation inputs being injected downstream of the flight control laws [7, 64]. The adverse consequences caused by operation of the flight control system on the system identification results are largely mitigated by following this approach.

### C. Flight Testing

Flight testing for system identification is executed in low-wind conditions to best adhere to modeling algorithm assumptions and improve modeling accuracy. This is particularly important at low speeds below where the air data sensors are reliable. To perform a system identification maneuver for RAVEN-SWFT, starting from a trimmed flight condition, the pilot reverses the polarity of a slider on the radio control (RC) transmitter to enable automated PTI excitations. The flight control system then injects the selected PTI into the control effector and/or reference commands, perturbing the vehicle around its reference operating conditions without requiring any additional pilot inputs.

While the PTI injections are running, the pilot still retains the ability to make stick inputs if the vehicle begins to significantly deviate from its nominal trajectory. Also, due to airspace constraints and ground-based pilot visual limitations, the pilot must turn the aircraft during longer duration system identification maneuvers (e.g., multisines) beyond hover. In the case where pilot inputs are needed, the pilot is requested to make corrections or turn using appropriate duration pulse inputs to avoid actively suppressing the PTIs. The necessary corrections are usually minimal because multisine inputs are symmetric about the trim settings. Once the desired maneuver duration has elapsed, the pilot disables the PTIs by returning the RC transmitter slider to its original position.

The type of the PTI injected by the flight control system is specified using RC transmitter channels and custom ground control station (GCS) parameters, as described further in Ref. [30]. Three RC transmitter switches are used to select the PTI type. To achieve an appropriate amount of vehicle excitation to obtain a good signal-to-noise ratio, the overall PTI amplitude is scaled using two rotary knobs on the RC transmitter: one knob to adjust control effector PTI amplitude and one knob to adjust reference command PTI amplitude. Furthermore, the individual reference command and control effector group amplitudes can be scaled separately by adjusting parameters on a GCS computer.

### D. Data Processing

After collecting the flight data, evaluation and processing steps are performed to prepare the data for model identification. System identification data processing procedures generally involve resampling, smoothing, correcting time delays, calculating unmeasured signals, and performing data compatibility analysis and corrections. For RAVEN-SWFT, the full-flight data are converted to have a constant 50 Hz sample rate, smoothed, used to calculate unmeasured signals (e.g., body-axis velocity, forces and moments), and placed into the SIDPAC flight data matrix format. The full-flight data are assessed using a strip chart viewer to investigate maneuver quality and determine precise maneuver start and end times. The sensor and state estimate kinematic consistency is then assessed for individual maneuvers. For the flight-state data, only minor accelerometer and rate gyro bias corrections were needed. For the control surface position and propulsor rotational speed measurements, time delay corrections were applied to synchronize these data with the state measurements. Control effector time delay corrections were made by synchronizing the flight control output commands, which are recorded alongside the state information on the Pixhawk, with the equivalent control effector commands from the servo-actuators and ESCs, which are stored on the external DAS along with the control surface positions and propulsor rotational speeds. The time delay correction was determined automatically using cross-correlation analysis.

### E. Model Identification

Model identification entails determining an appropriate model structure for each response and estimating unknown parameters in the model. Here, polynomial response surface equations (RSEs) are constructed to represent the response variables as a function of vehicle state and control variables. As presented and justified in Ref. [59], a full envelope model can be formed by developing sets of RSEs at several reference flight conditions. The response variables are the dimensional body-axis aero-propulsive forces $X, Y, Z$ in lbf and moments $L, M, N$ in ft·lbf. These variables, however, cannot be measured in flight and must be calculated from available sensors. The applied forces are computed as the product of the known vehicle mass and the body-axis translational acceleration at the aircraft center of gravity:

$$X = ma_x, \quad Y = ma_y, \quad Z = ma_z \tag{2}$$

The applied moments are computed using the known aircraft inertia tensor and measured angular velocity through the rotational dynamic equations augmented to include inertial coupling terms for rotating vehicle components:

$$L = I_x \dot{p} - I_{xz}\dot{r} + (I_z - I_y)qr - I_{xz}pq + \dot{h}_x + qh_z - rh_y \tag{3}$$

$$M = I_y \dot{q} + (I_x - I_z)pr + I_{xz}(p^2 - r^2) + \dot{h}_y + rh_x - ph_z \tag{4}$$

$$N = I_z \dot{r} - I_{xz}\dot{p} + (I_y - I_x)pq + I_{xz}qr + \dot{h}_z + ph_y - qh_x \tag{5}$$

The body-axis angular accelerations $\dot{p}, \dot{q}, \dot{r}$ are calculated using smoothed numerical differentiation of the body-axis angular velocity components [7, 65]. The explanatory variables are defined as the body-axis translational velocity components $u, v, w$ in ft/s; the time derivatives of body-axis velocity components $\dot{u}, \dot{v}, \dot{w}$ in ft/s$^2$; body-axis angular velocity components $p, q, r$ in rad/s; nacelle tilt angles $\delta_{t_1}, \delta_{t_2}, \delta_{t_3}, \delta_{t_4}$ in radians; flaperon deflection angles $\delta_{f_1}, \delta_{f_2}, \ldots, \delta_{f_6}$ in radians; stabilator deflection angle $\delta_s$ in radians; rudder deflection angle $\delta_r$ in radians; proprotor collective pitch angles $\delta_{c_1}, \delta_{c_2}, \ldots, \delta_{c_6}$ in radians; and squared proprotor rotational speeds $n_1^2, n_2^2, \ldots, n_6^2$ in rev$^2$/s$^2$. As discussed in Ref. [57], the proprotor rotational speed signals are squared because the thrust force from a proprotor is quadratically related to its rotational speed at a given flight condition. Accordingly, the squared proprotor rotational speeds represent linear changes in thrust production for each proprotor. To align with a multivariate Taylor series expansion formulation, each explanatory variable is centered on a reference value. Also, the $n_1^2, n_2^2, \ldots, n_6^2$ signals were normalized by $10^4$ to make the values, and associated parameter estimates, similar in magnitude to the other explanatory variables.

For this work, the model structure was determined using both multivariate orthogonal function (MOF) modeling [7, 66] and stepwise regression (SWR) [7, 67] in the time and frequency domains. Both linear and nonlinear model terms were considered for inclusion in the model. In the MOF modeling approach, candidate regressors are orthogonalized to enable assessment of the independent capability of each possible model term to describe the response variable variation. The candidate terms are ranked based on their improvement to the model and the terms that significantly contribute to the model are retained. For SWR, proposed model terms are sequentially added or removed from the model RSEs to determine which terms significantly improve the model performance.

For the final model structure, the unknown parameters were identified using complex least-squares regression [7, 68], which is a common frequency-domain equation-error method. The optimal estimate of unknown model parameters is calculated as

$$\hat{\boldsymbol{\theta}} = \left[ Re\left( \tilde{\boldsymbol{X}}^{\dagger} \tilde{\boldsymbol{X}} \right) \right]^{-1} Re\left( \tilde{\boldsymbol{X}}^{\dagger} \tilde{\boldsymbol{z}} \right) \tag{6}$$

where $\tilde{\boldsymbol{X}}$ is a matrix composed of complex regressors and $\tilde{\boldsymbol{z}}$ is the complex measured response vector. It is assumed that the regressors are error free and the measured response is only corrupted by constant variance, zero-mean, and uncorrelated error. $\tilde{\boldsymbol{X}}$ and $\tilde{\boldsymbol{z}}$ are computed by detrending the measured time-domain signals and transforming the variables into the frequency domain using a high-accuracy Fourier transform technique that allows for specification of an arbitrary frequency range $[f_{\text{min}}, f_{\text{max}}]$ and resolution $\Delta f$ [7, 69]. The standard error vector $\boldsymbol{s}(\hat{\boldsymbol{\theta}})$ corresponding to the identified parameter vector $\hat{\boldsymbol{\theta}}$ that accounts for an arbitrary analysis frequency range is determined as

$$\boldsymbol{s}(\hat{\boldsymbol{\theta}}) = \sqrt{\left( \frac{1}{2T\left(f_{\text{max}} - f_{\text{min}}\right)} Re\left[ \left( \tilde{\boldsymbol{z}} - \hat{\tilde{\boldsymbol{y}}} \right)^{\dagger} \left( \tilde{\boldsymbol{z}} - \hat{\tilde{\boldsymbol{y}}} \right) \right] \right) \ \operatorname{diag}\left( \left[ Re\left( \tilde{\boldsymbol{X}}^{\dagger} \tilde{\boldsymbol{X}} \right) \right]^{-1} \right)} \tag{7}$$

where $T$ is the maneuver duration and $\hat{\tilde{\boldsymbol{y}}} = \tilde{\boldsymbol{X}}\hat{\boldsymbol{\theta}}$ is the complex modeled response variable vector [68]. As a final step, the model equation bias term is determined as the mean value of the difference between the time-domain measured response $\boldsymbol{z}$ and modeled response $\hat{\boldsymbol{y}} = \boldsymbol{X}\hat{\boldsymbol{\theta}}$, where $\boldsymbol{X}$ is the time-domain regressor matrix [7, 68]. Additional specific parameter estimation implementation details will be discussed alongside the flight-test results shown later in the paper (Sec. VI).

### F. Model Validation

After completing model identification, the validation procedures are used to determine if the model is suitable for its intended purpose. Model adequacy is assessed by examining the identified parameters and the model prediction capability. Estimated model parameters should agree with physical intuition and have uncertainty values within acceptable limits. Model prediction accuracy is assessed using validation data withheld from the modeling process; the model predictions should closely follow the validation data with accuracy comparable to the model fit.

## V. Flight-Test Status

At the time of preparing this paper in Fall 2025, RAVEN-SWFT is actively undergoing transition envelope expansion flight testing. Partial transition flights have been accomplished up to a forward flight speed of 45 ft/s. Figure 9 shows photos of RAVEN-SWFT on a vertipad at the NASA Langley City Environment Range Testing for Autonomous Integrated Navigation (CERTAIN) flight-test range. Photos of the RAVEN-SWFT airborne in hover free-flight testing at the CERTAIN Range are displayed in Fig. 10.

RAVEN-SWFT flight testing has been composed of piloted assessment of the vehicle response, piloted doublets, automated square wave doublets, and automated multisine maneuvers to assess the performance of the flight control

Fig. 9 RAVEN-SWFT on a vertipad at the NASA Langley CERTAIN Range. (Credit: NASA)

Fig. 10 RAVEN-SWFT hover free-flight testing. (Credit: NASA)

system and to collect data for system identification. The flight-test research conducted on RAVEN-SWFT started immediately, including enabling the 28-signal multisine PTI described in Sec. IV.B on the very first free flight of the aircraft.

Since the publication of Ref. [30] in May 2025, envelope expansion flight testing has revealed critical insights that have improved the flight control system. Transition flight tests revealed challenging aero-propulsive interaction effects that occur in a limited airspeed range starting around 30 ft/s, leading to an adverse pitching motion. Using flow visualization tufts installed on the aircraft and an onboard camera (shown in Fig. 9), alongside transition flight testing with different trim stabilator angles, this phenomenon was found to be connected to proprotor slipstream interactions with the stabilator. To mitigate the phenomenon, the stabilator trim was adjusted to have significant trailing edge down deflection around the affected airspeeds. Flight testing has also yielded data that have aided in the development and refinement of the turn coordination methodology in the transition regime, adjustment of flight control and allocation tuning parameters, modification of the trim strategy, and characterization of aircraft instrumentation to improve flight control logic.

Flight testing is expected to continue gradually expanding the flight envelope through a full transition into forward flight. At multiple conditions throughout the RAVEN-SWFT transition envelope, flight data are planned to be collected with multisine PTI injections active to develop a transition aero-propulsive model that can be used for comparison, adjustment, or replacement of the baseline RAVEN-SWFT aero-propulsive model. At the time of writing this paper, system identification testing has been conducted in hover and early transition flight conditions. The system identification results described next focus on the hover flight condition.

## VI. Hover System Identification Results

This section describes the RAVEN-SWFT system identification results and findings specific to the hover flight regime. The flight-test maneuvers used for model identification, the aero-propulsive model structure, and the final modeling results are presented.

### A. Flight-Test Maneuvers

Multiple maneuver variations were considered and studied for hover system identification for the RAVEN-SWFT aircraft. Two maneuver types applying the multisine input excitations, shown in Figs. 7-8, were preferred and used for system identification in this paper. In the first maneuver type, the reference command ($\eta_{\text{lon}}$, $\eta_{\text{lat}}$, $\eta_{\text{dir}}$, $\eta_{\text{ver}}$) multisine signal amplitudes were set to zero. In other words, multisine signals were only applied to 24 independent control effectors; thus, this maneuver is referred to as the control effector (CE) multisine maneuver. Figure 11 shows the flight data collected during a sample hover CE multisine maneuver. For the second maneuver type, the 24 control effector and 4 reference command multisine signals were active and is, accordingly, referred to as the reference command and control effector (RC+CE) multisine maneuver. Flight data from an example hover RC+CE multisine maneuver are shown in Fig. 12. Due to the active flight control system, the control effector signals are distorted from the designed multisine excitations in each maneuver type (cf. Fig. 8); however, the signals remain sufficiently decorrelated for model identification as a result of the input injection strategy shown in Fig. 6. Figures 13-14 show the pairwise correlation coefficients and cross plots for the explanatory variables defined in Sec. IV.E for each example maneuver. The CE and RC+CE multisine maneuvers were each found to have unique utility for model identification.

For the CE multisine maneuver, the control effector signal amplitudes were able to be increased higher than the same control effector signals in RC+CE maneuver, while still permitting safe flight operations. The larger control effector multisine amplitudes cause a larger vehicle response attributed to independent control effector perturbations, allowing the control effector parameter estimates to be more accurately identified. The improved control effector parameter estimation accuracy, however, was achieved at the expense of less accurate estimates for certain state parameters. This reflects the findings discussed in Refs. [57, 60]. In these studies, system identification maneuvers with multisine signals only applied to the control effectors—without supplementary deliberate state excitation—were reported to not invoke adequate state perturbations for accurate identification of certain state derivatives at low flight speeds. For RAVEN-SWFT hover flight testing, in particular, the $u$, $v$, $w$, and $r$ signals were found to not be sufficiently excited for accurate estimation of their associated model parameters in hover.

As a mitigation for the deficient state excitation observed for the CE multisine in hover, additional deliberate state command injections are required. This could, for example, be automated or piloted single-axis multistep inputs that are applied while multisine signals are active. Piloted doublet excitation sequences applied with multisine inputs being active on the control effectors were executed for an industry vectored-thrust prototype eVTOL aircraft in Ref. [57]. A similar approach of piloted excitations applied alongside multisine excitations was described for a multirotor system identification effort in Ref. [53]. Incorporating both piloted and automated doublet inputs executed in parallel to control effector multisine inputs was also explored with RAVEN-SWFT. Although this is an acceptable approach, it was found that applying the RC+CE multisine was superior in terms of efficiency, data information content, and identification accuracy. The RAVEN-SWFT pilots also preferred the fully-automated maneuvers, which reduced pilot workload and allowed the pilot to focus on safe operation of the vehicle. The downside of the RC+CE maneuver is that, to achieve sufficient $u$, $v$, $w$, and $r$ excitation through increased reference command multisine signal amplitudes, the control effector multisine signal amplitudes needed to be lower compared to the CE multisine to maintain safe flight operations. As a result, this maneuver improved estimation of parameters related to the $u$, $v$, $w$, and $r$ state variables, at the expense of less accurate control effectiveness parameter estimation. The signal amplitude trade-offs can be seen by comparing Figs. 11-12. In Fig. 11, the control effector actuation range is larger, whereas the ranges of the $u$, $v$, $w$, and $r$ signals are larger in Fig. 12.

The dual CE and RC+CE multisine maneuver execution approach and the forthcoming parameter estimation approach was found to work well for system identification of the RAVEN-SWFT aircraft in hover. To study repeatability and improve parameter estimation accuracy for this research investigation, several repeats of each maneuver type that lasted approximately 60 seconds were collected in hover and used for modeling. However, acquiring several repeated maneuvers is unnecessary in practice, where single or few well-executed approximately 60-second multisine maneuvers can facilitate accurate modeling.

From the results in this study and prior work [57, 60], there is considerable evidence that supplementing control effector multisine signals with additional intentional state perturbations is needed to achieve adequate state derivative identification at low speeds for eVTOL vehicles. In other words, the CE multisine maneuver alone is inadequate to address all eVTOL hover system identification objectives, where accurate state and control derivatives are desired. Although two different types of multisine maneuvers were found to be helpful for RAVEN-SWFT system identification in hover, this dual maneuver approach may not be required for different eVTOL aircraft configurations and sizes. In many cases, it is anticipated that using a single RC+CE multisine maneuver for eVTOL vehicle system identification would be adequate.

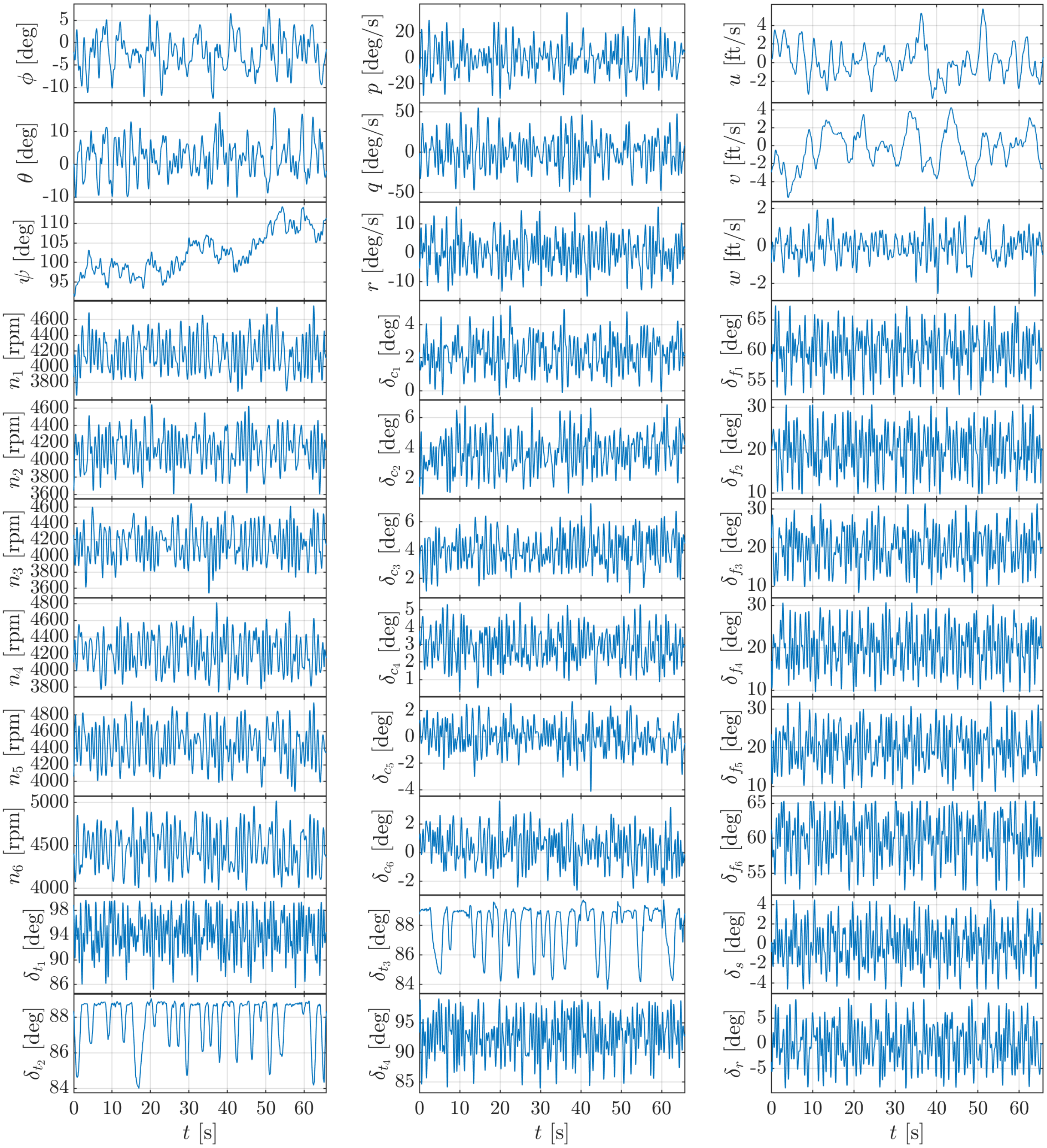

**Fig. 11 Example flight data from a hover CE multisine maneuver.**

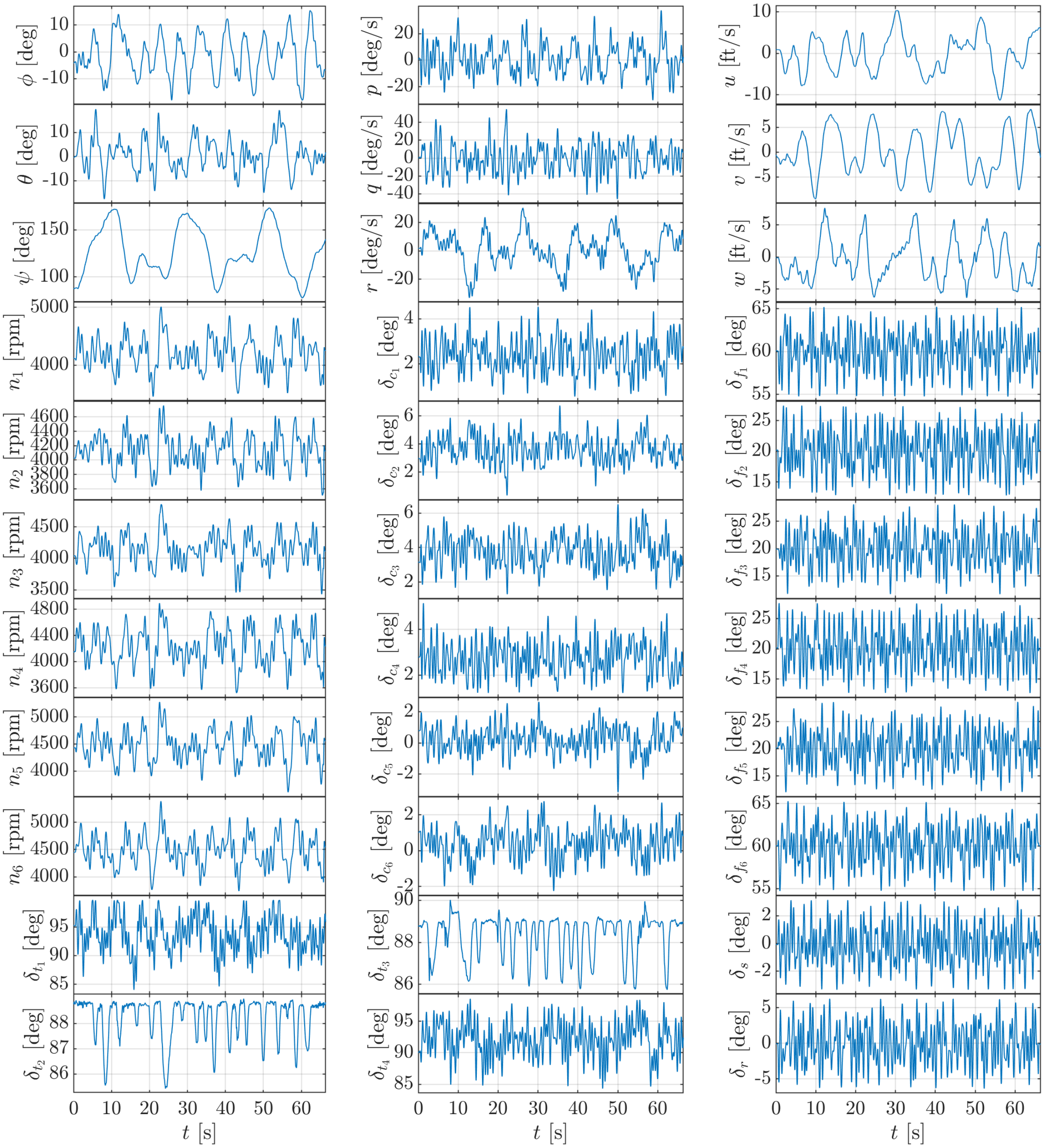

Fig. 12 Example flight data from a hover RC+CE multisine maneuver.

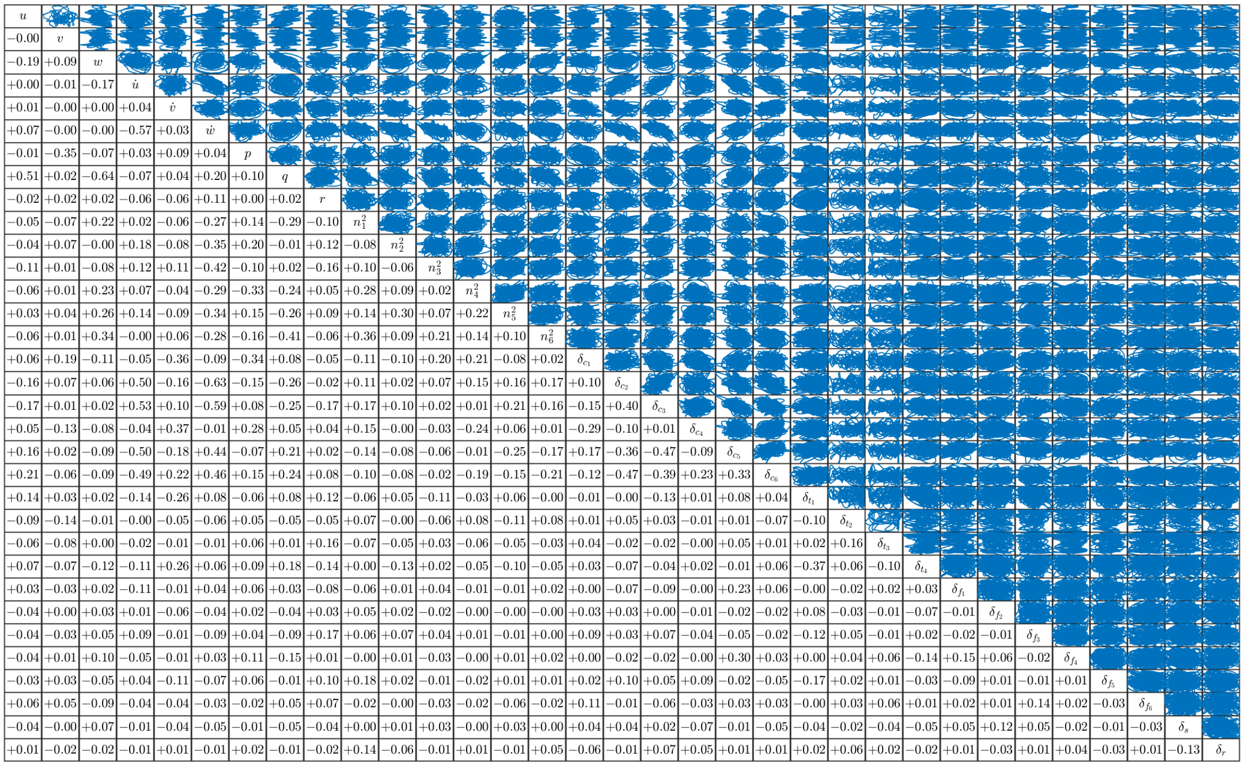

**Fig. 13 Explanatory variable cross plots and correlation coefficients for a hover CE multisine maneuver.**

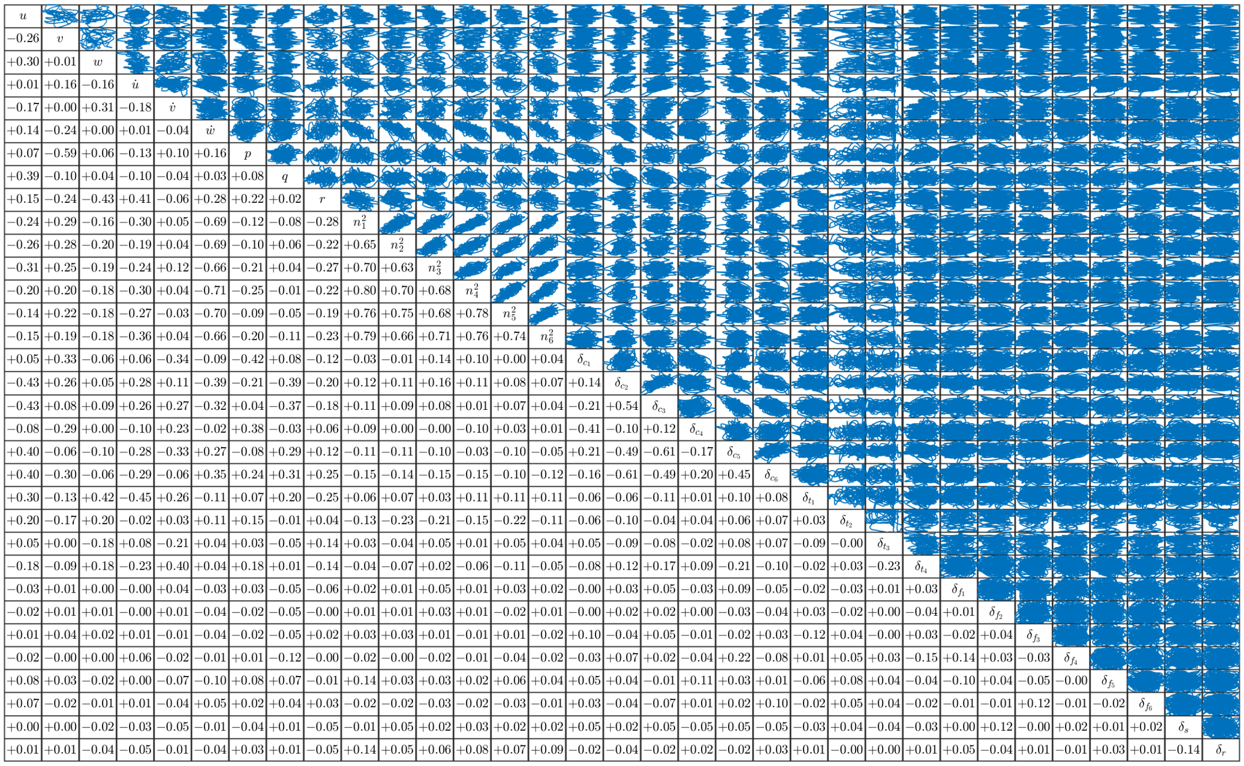

**Fig. 14 Explanatory variable cross plots and correlation coefficients for a hover RC+CE multisine maneuver.**

### B. Model Structure

As mentioned in Sec. IV.E, the model structure was determined with complementary use of both the MOF [7, 66] and SWR [7, 67] algorithms in the time and frequency domains. Prioritization was given to model terms linear in the defined explanatory variables, but certain nonlinear terms were also considered: pure quadratic body-axis velocity variables ($u^2$, $v^2$, $w^2$), cross translational and angular velocity variables (e.g., $vp$, $uq$, $wr$), and certain control effector interaction terms based on the vehicle configuration (e.g., $n_1^2\delta_{t_1}$, $n_4^2\delta_{f_6}$, $\delta_{c_2}\delta_{t_2}$). First, MOF was applied to each flight maneuver to determine the candidate regressors that appeared in a majority of the flight maneuvers. Then, based on findings from MOF, SWR was applied to review fringe model terms using statistical metrics, as well as physical insight into the aero-propulsive modeling problem, to finalize the aero-propulsive model structure.

After determining the model structure, the model equations were symmetrized to form a final model structure. Mirrored control effectors over the $x$–$z$ plane are expected to have the same magnitude in their parameter estimates, but are generally not estimated to be equal because of small physical geometric asymmetries in vehicle fabrication and modeling error. Because simulation and control applications often prefer to have equal effectiveness for mirrored control effectors, the models were symmetrized by constraining mirrored control parameters to have equal magnitude in the parameter estimation approach. Parameter symmetrization was implemented by adding or subtracting the centered control effector values, as determined by the relative signs of the isolated parameter estimates. The result is a combined regressor enabling estimation of the symmetrized control effectiveness. Following similar justification, the bias parameters for the lateral-directional response were estimated by the identification approach, but were discarded so that the aerodynamics are symmetric in the $x$–$z$ plane in the final model.

The RAVEN-SWFT symmetrized hover model structure for each aero-propulsive force and moment was determined to be:

$$\begin{aligned} X = {} & X_u u + X_w w + X_{wq} wq + X_{\delta_{f_{16}}}(\delta_{f_1} + \delta_{f_6}) + X_{\delta_{t_{14}}}(\delta_{t_1} + \delta_{t_4}) + X_{\delta_{t_{23}}}(\delta_{t_2} + \delta_{t_3}) + X_{\delta_{c_{23}}}(\delta_{c_2} + \delta_{c_3}) \\ & + X_{\delta_{c_{56}}}(\delta_{c_5} + \delta_{c_6}) + X_{n_{23}^2}(n_2^2 + n_3^2) + X_{n_{56}^2}(n_5^2 + n_6^2) + X_{n_{14}^2\delta_{t_{14}}}(n_1^2\delta_{t_1} + n_4^2\delta_{t_4}) + X_{n_{23}^2\delta_{t_{23}}}(n_2^2\delta_{t_2} + n_3^2\delta_{t_3}) \\ & + X_{\delta_{c_{14}}\delta_{t_{14}}}(\delta_{c_1}\delta_{t_1} + \delta_{c_4}\delta_{t_4}) + X_{\delta_{c_{23}}\delta_{t_{23}}}(\delta_{c_2}\delta_{t_2} + \delta_{c_3}\delta_{t_3}) + X_o \end{aligned} \tag{8}$$

$$\begin{aligned} Y = {} & Y_v v + Y_{\delta_{t_{14}}}(\delta_{t_1} - \delta_{t_4}) + Y_{\delta_{t_{23}}}(\delta_{t_2} - \delta_{t_3}) + Y_{\delta_{c_{14}}}(\delta_{c_1} - \delta_{c_4}) + Y_{\delta_{c_{23}}}(\delta_{c_2} - \delta_{c_3}) + Y_{\delta_{c_{56}}}(\delta_{c_5} - \delta_{c_6}) \\ & + Y_{n_{14}^2}(n_1^2 - n_4^2) + Y_{n_{23}^2}(n_2^2 - n_3^2) + Y_{n_{56}^2}(n_5^2 - n_6^2) \end{aligned} \tag{9}$$

$$\begin{aligned} Z = {} & Z_w w + Z_{uq} uq + Z_{vp} vp + Z_{\dot{w}} \dot{w} + Z_{\delta_{c_{14}}}(\delta_{c_1} + \delta_{c_4}) + Z_{\delta_{c_{23}}}(\delta_{c_2} + \delta_{c_3}) + Z_{\delta_{c_{56}}}(\delta_{c_5} + \delta_{c_6}) + Z_{n_{14}^2}(n_1^2 + n_4^2) \\ & + Z_{n_{23}^2}(n_2^2 + n_3^2) + Z_{n_{56}^2}(n_5^2 + n_6^2) + Z_o \end{aligned} \tag{10}$$

$$\begin{aligned} L = {} & L_v v + L_p p + L_{wr} wr + L_{vr} vr + L_{\delta_{f_{16}}}(\delta_{f_1} - \delta_{f_6}) + L_{\delta_{t_{14}}}(\delta_{t_1} - \delta_{t_4}) + L_{\delta_{c_{14}}}(\delta_{c_1} - \delta_{c_4}) + L_{\delta_{c_{23}}}(\delta_{c_2} - \delta_{c_3}) \\ & + L_{\delta_{c_{56}}}(\delta_{c_5} - \delta_{c_6}) + L_{n_{14}^2}(n_1^2 - n_4^2) + L_{n_{23}^2}(n_2^2 - n_3^2) + L_{n_{56}^2}(n_5^2 - n_6^2) \end{aligned} \tag{11}$$

$$\begin{aligned} M = {} & M_u u + M_w w + M_{uq} uq + M_{wq} wq + M_{vp} vp + M_{\dot{w}} \dot{w} + M_{\delta_{c_{23}}}(\delta_{c_2} + \delta_{c_3}) + M_{\delta_{c_{56}}}(\delta_{c_5} + \delta_{c_6}) \\ & + M_{n_{23}^2}(n_2^2 + n_3^2) + M_{n_{56}^2}(n_5^2 + n_6^2) + M_o \end{aligned} \tag{12}$$

$$\begin{aligned} N = {} & N_r r + N_{\delta_{f_{16}}}(\delta_{f_1} - \delta_{f_6}) + N_{\delta_{t_{14}}}(\delta_{t_1} - \delta_{t_4}) + N_{\delta_{t_{23}}}(\delta_{t_2} - \delta_{t_3}) + N_{\delta_{c_{14}}}(\delta_{c_1} - \delta_{c_4}) + N_{\delta_{c_{23}}}(\delta_{c_2} - \delta_{c_3}) \\ & + N_{n_{14}^2}(n_1^2 - n_4^2) + N_{n_{23}^2}(n_2^2 - n_3^2) + N_{n_{14}^2\delta_{t_{14}}}(n_1^2\delta_{t_1} - n_4^2\delta_{t_4}) + N_{\delta_{c_{14}}\delta_{t_{14}}}(\delta_{c_1}\delta_{t_1} - \delta_{c_4}\delta_{t_4}) \\ & + I_p\left(\textstyle\sum_{i=1}^{6}(-1)^i\dot{\Omega}_i\right) \end{aligned} \tag{13}$$

The model structure is nonlinear, including cross translational velocity and angular velocity terms as well as control effector interaction terms found to be significant. The midboard flaperon ($\delta_{f_2}, \delta_{f_5}$), inboard flaperon ($\delta_{f_3}, \delta_{f_4}$), stabilator ($\delta_s$), and rudder ($\delta_r$) deflection effects were found to be insignificant due to a lack of proprotor slipstream interactions with these control surfaces and limited freestream airflow near hover. Although it may be possible to neglect rotating vehicle component inertial coupling terms in the rotational dynamics equations [Eqs. (3)-(5)] due to their small contributions relative to the applied aero-propulsive moments, it was found that the moment of inertia of the rotating propulsor, $I_p$, could be estimated in the yawing moment from the transient torque effects aligned with the $z$ axis, as shown in Eq. (13). Propulsor gyroscopic effects were found to be insignificant in the rolling and pitching moment equations.

### C. Parameter Estimation

The final model parameters for each maneuver were obtained using complex least-squares regression [7, 68]. To reserve data for model validation, the last 10 seconds of data were withheld from the modeling process in each maneuver, leaving the remaining portion of the maneuver available for parameter estimation. For a general aircraft system identification problem, use of validation data with an input waveform that differs from the data used for modeling is considered a best practice; however, due to the large number of control effectors ubiquitous with eVTOL aircraft, it is cumbersome to implement a practical and rigorous prediction test. For this reason, data used for modeling and validation were both from multisine maneuvers, but each from different portions of the maneuver to have validation data character differences relative to the modeling data.

The data from individual CE and RC+CE multisine maneuvers were used to estimate the parameters in the hover model structure [Eqs. (8)-(13)]. Figure 15 shows the frequency-domain model fits to the example CE and RC+CE multisine maneuver flight data presented in Figs. 11-12. The frequency-domain coefficient of determination ($R^2$), which quantifies response variable variation captured by the model, is shown on the subplot for each response. For the CE multisine maneuver (Fig. 15a), good model fits and high $R^2$ values above 93% are observed for $Z$, $L$, $M$, and $N$. The $X$ response is observed to have a slightly degraded but still adequate model fit, with further degradation seen for $Y$, which is explained by less direct control excitation in these responses in hover. For the RC+CE multisine maneuver (Fig. 15b), the model fits in $X$, $Y$, and $Z$ are improved and the model fits are degraded for $L$, $M$, and $N$, relative to the CE multisine maneuver. The RC+CE multisine maneuver clearly exhibits larger magnitude low-frequency content, as a result of the low-frequency supplemental reference command multisine inputs. The model fits in the time domain for the same example multisine maneuvers are shown in Fig. 16, which use the model parameters estimated for each maneuver in the frequency domain. The closeness of the time-domain model fits resemble the observations in the frequency domain. Similar model identification results were obtained for the repeated CE and RC+CE maneuvers. Figure 17 gives the average frequency-domain $R^2$ for each response obtained from analysis of CE and RC+CE multisine maneuvers. Reflecting the results seen in the example maneuvers, the average $R^2$ values are higher in $L$, $M$, and $N$ for the CE multisine maneuver and higher in $X$, $Y$, and $Z$ for the RC+CE multisine maneuver.

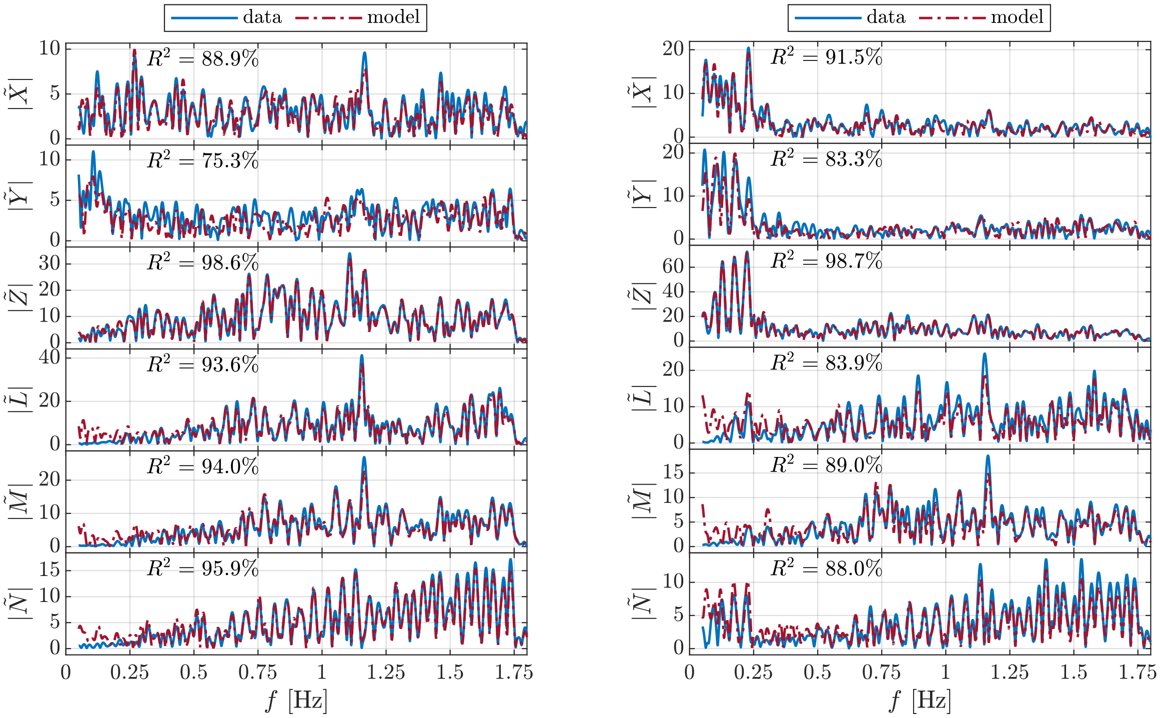

**(a) CE multisine maneuver**

**(b) RC+CE multisine maneuver**

**Fig. 15 Frequency-domain response data and model fit for example hover flight maneuvers.**

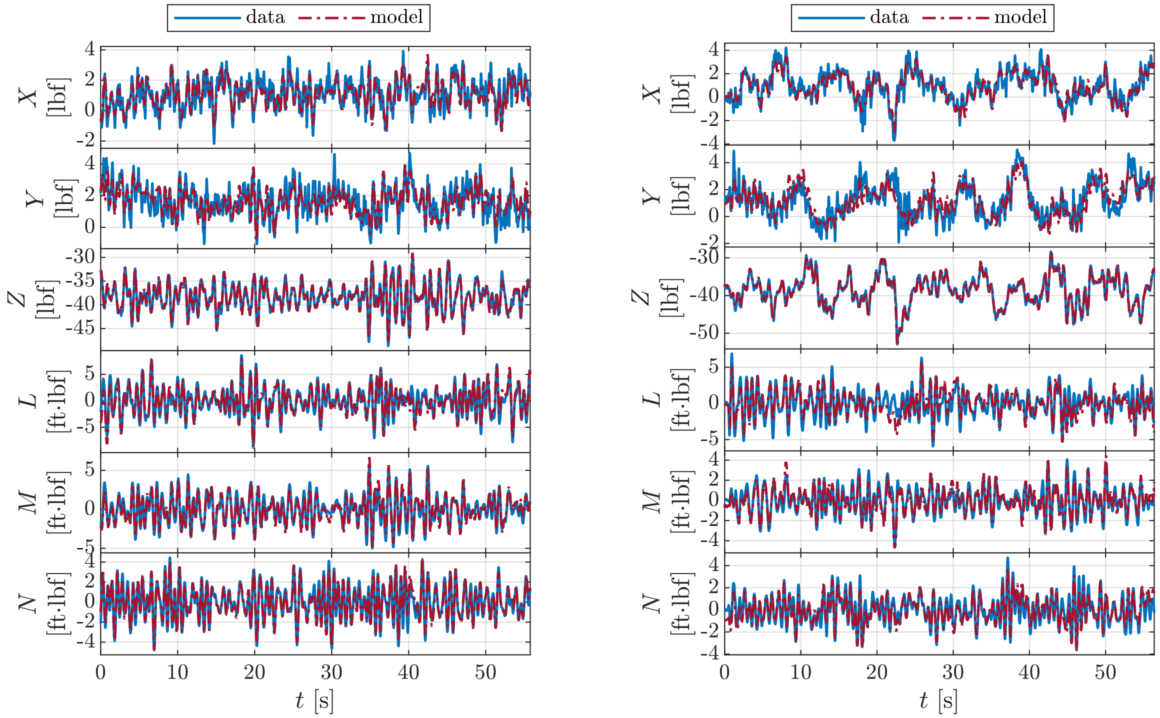

**(a) CE multisine maneuver** **(b) RC+CE multisine maneuver**

**Fig. 16 Time-domain smoothed response data and model fit for example hover multisine maneuvers.**

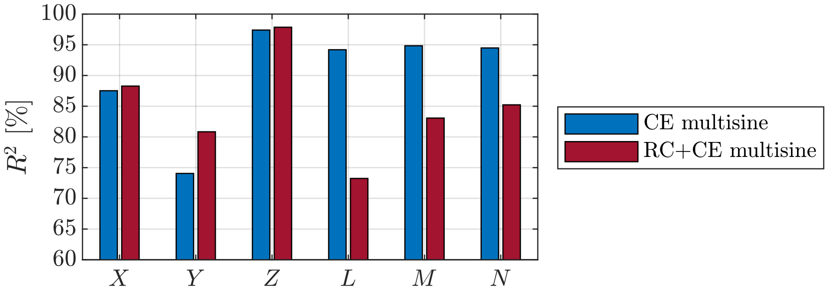

**Fig. 17 Average coefficient of determination, $R^2$, for model identification from each maneuver type.**

### D. Final Combined Model

The process to determine the hover parameter estimates included in the final model reflected the system identification flight-test approach and individual maneuver parameter estimation findings. As described previously, model identification from CE multisine maneuvers was found to yield more accurate and repeatable control effectiveness parameter estimates; however, the parameters associated with certain state variables ($u$, $v$, $w$, $r$) were not accurately identified due to insufficient excitation of these states during the maneuver. In contrast, the RC+CE multisine maneuvers have larger, more informative variation of the $u$, $v$, $w$, and $r$ state variables leading to more accurate identification of their associated parameters, but at the expense of less accurate control effectiveness estimates.

Multiple approaches to combine the complementary information content in each maneuver type were considered: selective parameter extraction from each maneuver type analyzed independently, constrained sequential estimation, parameter estimation from concatenated maneuvers, and sequential Bayesian parameter estimation. Selective parameter extraction was ultimately chosen for its ability to directly incorporate engineering insight pertaining to parameter estimation quality based on maneuver excitation character, as well as its resilience to maneuvers with different complicating atmospheric disturbances and noise characteristics. The approach also avoids issues that can arise in the alternative approaches: corruption from estimation bias propagated between sequential identification steps, adverse parameter averaging using deficient information, and constraints that can degrade parameter estimation accuracy. The selective parameter extraction approach inherently assumes that the parameters are sufficiently decorrelated, which is achieved through the application of multisine signals during the maneuvers used for model identification and is supported by the correlation analysis presented in Figs. 13-14. Although it is recognized that alternative methods offer superior mathematical elegance, the selective parameter extraction approach was determined to be the most appropriate practical methodology for model development given the characteristics of the analyzed flight test data.

To implement the selective parameter extraction approach, the final parameter values were determined by combining parameter estimates from separate flight maneuvers using the weighted mean

$$\hat{\theta} = \frac{\sum_{i=1}^{n} \left[\hat{\theta}_i / s_i^2\right]}{\sum_{i=1}^{n} \left[1 / s_i^2\right]} \tag{14}$$

with associated propagated uncertainty estimate [70]:

$$\sigma = \sqrt{\frac{1}{\sum_{i=1}^{n} \left[1 / s_i^2\right]}} \tag{15}$$

In these equations, $\hat{\theta}_i$ is a scalar parameter estimate for the $i$th maneuver, $s_i$ is the corresponding $i$th scalar standard error estimate, and $n$ is the number of independent flight maneuvers. Parameters for regressors including $u$, $v$, $w$, or $r$ were combined from RC+CE multisine maneuvers, whereas all other non-bias parameters were combined from CE multisine maneuvers. The final bias parameters were combined from both maneuver types. The parameter estimates in the final combined model generally have low uncertainty values, with a majority of the parameters having less than 5% error, while also demonstrating reasonable agreement with prior modeling results and consistency with physical intuition.

To assess the final combined model, the model predictions were compared to the original smoothed aero-propulsive force and moment response data for each maneuver, including the data withheld for model validation. Figures 18 and 19 show the model predictions for the example CE and RC+CE multisine maneuvers compared to the modeling data in the first part of the maneuver and validation data comprising the last 10 seconds of the maneuver. The model outputs closely follow the data used for modeling, with similar prediction quality to the modeling performed using individual maneuvers shown in Fig. 16. The model outputs predict the validation data with similar success.

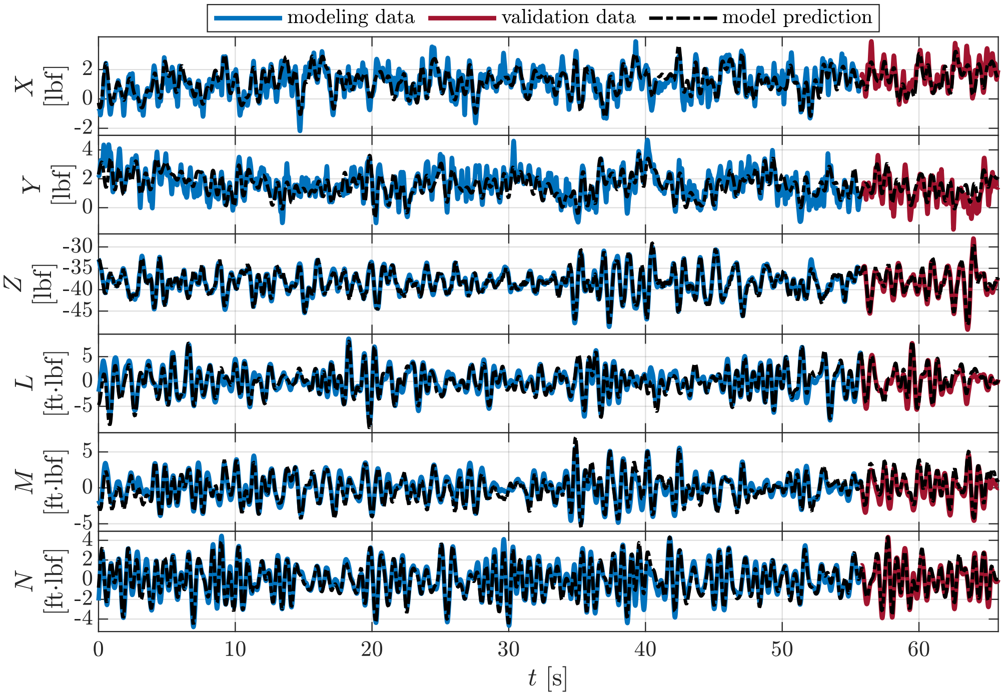

**Fig. 18 Comparison of smoothed response data and final model prediction for a hover CE multisine maneuver.**

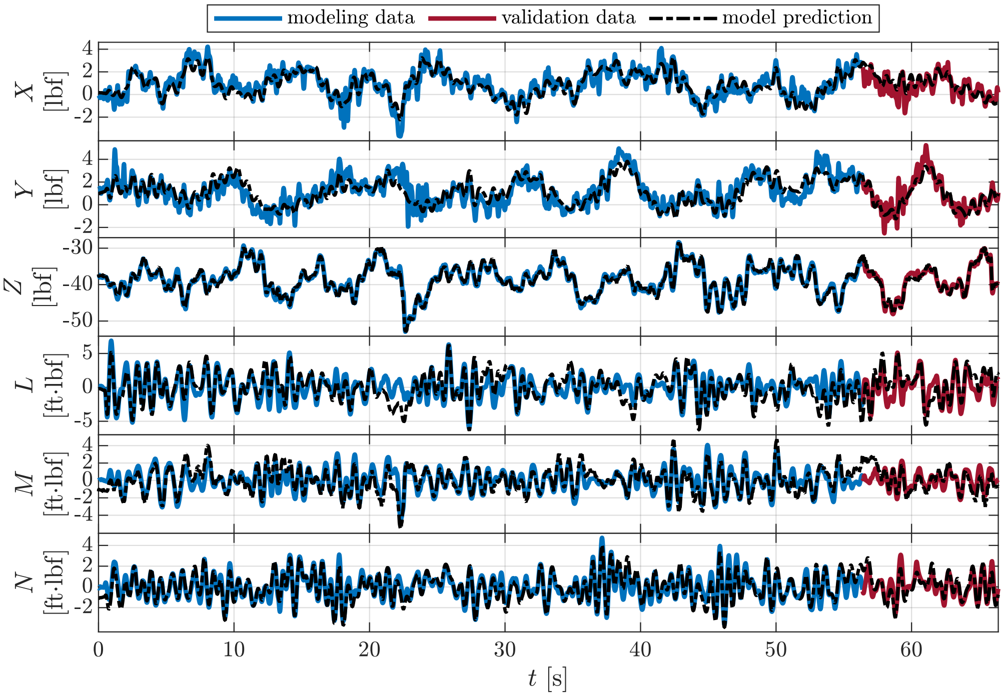

**Fig. 19 Comparison of smoothed response data and final model prediction for a hover RC+CE multisine maneuver.**

The normalized root-mean-square error (NRMSE) metric was used to further quantitatively compare the final model prediction performance for modeling and validation data. The percentage NRMSE is calculated as:

$$\text{NRMSE} = 100 \times \frac{1}{\text{range}(z_m)} \sqrt{\frac{(z - \hat{y})^T (z - \hat{y})}{N}} \tag{16}$$

Here, $z$ is the response data vector in the time domain and $\hat{y}$ is the corresponding model prediction vector, which each have a length of $N$ data points. Normalization is performed based on the range of the measured response used for model identification [$\text{range}(z_m) = \max(z_m) - \min(z_m)$] for both the modeling NRMSE and validation NRMSE. Figure 20 shows the NRMSE computed using modeling and validation data for each multisine maneuver type. For each maneuver, the modeling and validation NRMSE values are low and similar in value, supporting that the final model has good prediction abilities.

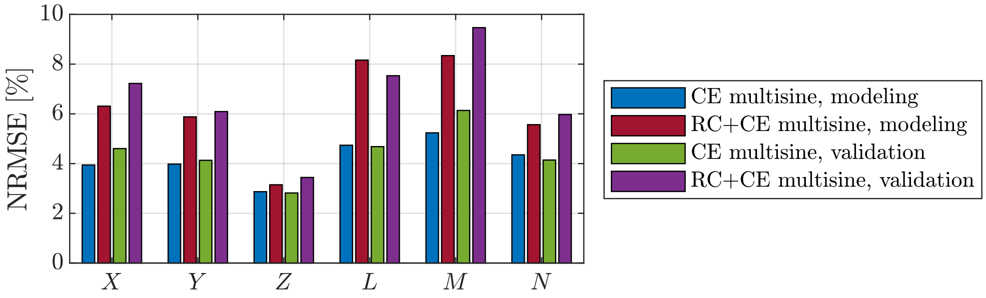

**Fig. 20 Modeling and validation NRMSE for each maneuver type.**

# VII. Conclusions

Accurate dynamic models are needed by multiple disciplines to enable successful realization of operational eVTOL vehicles. These aircraft, however, present challenges to efficient and accurate aero-propulsive model development, including many control effectors to characterize, significant aero-propulsive coupling, and a vast flight envelope with substantially varying aerodynamics. Building on foundational wind-tunnel testing and simulated flight testing efforts, this paper presented a flight-test system identification approach for the NASA RAVEN-SWFT tiltrotor eVTOL aircraft. The presented results focused on model development from hover flight testing.

The flight-test experiment design involved applying orthogonal phase-optimized multisine inputs to the individual control effectors, as well as translational velocity and yaw rate reference commands. Two multisine maneuver types were shown for hover system identification and were each found to have advantages and drawbacks for the RAVEN-SWFT hover modeling effort. A key finding was that the supplemental reference command multisine inputs help to supply sufficient excitation in the translational velocity components and yaw rate signals in the hover flight regime for accurate identification of associated parameters. Modeling results were presented for individual hover maneuvers and a combined final hover model, which showed that the identified models have good prediction capability.

The overall system identification strategy facilitates efficient and accurate modeling of complex eVTOL aircraft using flight testing performed throughout the transition envelope. Although only hover system identification results were presented in this paper, the utility and practicality of the approach were evident. Accordingly, the system identification approach is recommended for current and future eVTOL aircraft modeling efforts using flight test data.

# Acknowledgments

This research was funded by the NASA Aeronautics Research Mission Directorate (ARMD) Transformational Tools and Technologies (TTT) project and Flight Demonstrations and Capabilities (FDC) project. RAVEN-SWFT vehicle development and flight-test support was provided by Gregory Howland, Matthew Gray, Jody Miller, Brayden Chamberlain, Ryan Chan, David North, Steven Geuther, Justin Lisee, and Gary Banziger. Discussions with the RAVEN-SWFT pilots, Jody Miller and Brayden Chamberlain, helped to form the final flight-test strategy. Flight-test operations and authorization support was provided by Matthew Coldsnow, Jontae Park, Jennifer Fowler, Dustin Schmitt, Patrick Hill, Jacob Schaefer, and Matthew Underwood. Other members of the RAVEN project who contributed to the RAVEN-SWFT vehicle development, flight control system development, and flight testing include: Garrett Asper, Rachel Axten, Steven Snyder, Ronald Busan, Michael Acheson, Stephen Riddick, Jacob Cook, Jacob Schaefer, Siena Whiteside, and Jason Welstead. The contributions from all team members are gratefully acknowledged and appreciated.

# References

[1] Johnson, W., Silva, C., and Solis, E., "Concept Vehicles for VTOL Air Taxi Operations," *AHS Technical Conference on Aeromechanics Design for Transformative Vertical Flight*, Jan. 2018.

[2] Silva, C., Johnson, W., Antcliff, K. R., and Patterson, M. D., "VTOL Urban Air Mobility Concept Vehicles for Technology Development," *2018 Aviation Technology, Integration, and Operations Conference*, AIAA Paper 2018-3847, Jun. 2018. https://doi.org/10.2514/6.2018-3847.

[3] Kim, H. D., Perry, A. T., and Ansell, P. J., "A Review of Distributed Electric Propulsion Concepts for Air Vehicle Technology," *2018 AIAA/IEEE Electric Aircraft Technologies Symposium*, AIAA Paper 2018-4998, Jul. 2018. https://doi.org/10.2514/6.2018-4998.

[4] Saeed, A. S., Younes, A. B., Cai, C., and Cai, G., "A Survey of Hybrid Unmanned Aerial Vehicles," *Progress in Aerospace Sciences*, Vol. 98, 2018, pp. 91–105. https://doi.org/10.1016/j.paerosci.2018.03.007.

[5] Johnson, W., and Silva, C., "NASA Concept Vehicles and the Engineering of Advanced Air Mobility Aircraft," *The Aeronautical Journal*, Vol. 126, No. 1295, 2022, pp. 59–91. https://doi.org/10.1017/aer.2021.92.

[6] "eVTOL Aircraft Directory," *Electric VTOL News™*, https://evtol.news/aircraft, Accessed 23 November 2025.

[7] Morelli, E. A., and Klein, V., *Aircraft System Identification: Theory and Practice*, 2nd ed., Sunflyte Enterprises, Williamsburg, VA, 2016.

[8] Jategaonkar, R. V., *Flight Vehicle System Identification: A Time-Domain Methodology*, 2nd ed., American Institute of Aeronautics and Astronautics, Reston, VA, 2015. https://doi.org/10.2514/4.102790.

[9] Tischler, M. B., and Remple, R. K., *Aircraft and Rotorcraft System Identification: Engineering Methods With Flight-Test Examples*, $2^{\text{nd}}$ ed., American Institute of Aeronautics and Astronautics, Reston, VA, 2012. https://doi.org/10.2514/4.868207.

[10] Jategaonkar, R., Fischenberg, D., and von Gruenhagen, W., "Aerodynamic Modeling and System Identification from Flight Data-Recent Applications at DLR," *Journal of Aircraft*, Vol. 41, No. 4, 2004, pp. 681–691. https://doi.org/10.2514/1.3165.

[11] Wang, K. C., and Iliff, K. W., "Retrospective and Recent Examples of Aircraft Parameter Identification at NASA Dryden Flight Research Center," *Journal of Aircraft*, Vol. 41, No. 4, 2004, pp. 752–764. https://doi.org/10.2514/1.332.

[12] Morelli, E. A., and Klein, V., "Application of System Identification to Aircraft at NASA Langley Research Center," *Journal of Aircraft*, Vol. 42, No. 1, 2005, pp. 12–25. https://doi.org/10.2514/1.3648.

[13] Morelli, E. A., and Grauer, J. A., "Advances in Aircraft System Identification at NASA Langley Research Center," *Journal of Aircraft*, Vol. 60, No. 5, 2023, pp. 1354–1370. https://doi.org/10.2514/1.C037274.

[14] Berger, T., Tobias, E. L., Tischler, M. B., and Juhasz, O., "Advances and Modern Applications of Frequency-Domain Aircraft and Rotorcraft System Identification," *Journal of Aircraft*, Vol. 60, No. 5, 2023, pp. 1331–1353. https://doi.org/10.2514/1.C037275.

[15] Deiler, C., Mönnich, W., Seher-Weiß, S., and Wartmann, J., "Retrospective and Recent Examples of Aircraft and Rotorcraft System Identification at DLR," *Journal of Aircraft*, Vol. 60, No. 5, 2023, pp. 1371–1397. https://doi.org/10.2514/1.C037262.

[16] Geuther, S. C., Simmons, B. M., and Ackerman, K. A., "Overview of the Subscale RAVEN Flight Controls and Modeling Testbed," *Vertical Flight Society's 80th Annual Forum & Technology Display*, May 2024. https://doi.org/10.4050/F-0080-2024-1185.

[17] German, B. J., Jha, A., Whiteside, S. K. S., and Welstead, J. R., "Overview of the Research Aircraft for eVTOL Enabling techNologies (RAVEN) Activity," *AIAA AVIATION 2023 Forum*, AIAA Paper 2023-3924, June 2023. https://doi.org/10.2514/6.2023-3924.

[18] Rothhaar, P. M., Murphy, P. C., Bacon, B. J., Gregory, I. M., Grauer, J. A., Busan, R. C., and Croom, M. A., "NASA Langley Distributed Propulsion VTOL Tilt-Wing Aircraft Testing, Modeling, Simulation, Control, and Flight Test Development," *14th AIAA Aviation Technology, Integration, and Operations Conference*, AIAA Paper 2014-2999, Jun. 2014. https://doi.org/10.2514/6.2014-2999.

[19] McSwain, R. G., Geuther, S. C., Howland, G., Patterson, M. D., Whiteside, S. K., and North, D. D., "An Experimental Approach to a Rapid Propulsion and Aeronautics Concepts Testbed," NASA TM–2020-220437, Jan. 2020.

[20] North, D. D., Busan, R. C., and Howland, G., "Design and Fabrication of the Langley Aerodrome No. 8 Distributed Electric Propulsion VTOL Testbed," *AIAA SciTech 2021 Forum*, AIAA Paper 2021-1188, Jan. 2021. https://doi.org/10.2514/6.2021-1188.

[21] Busan, R. C., Rothhaar, P. M., Croom, M. A., Murphy, P. C., Grafton, S. B., and O'Neal, A. W., "Enabling Advanced Wind-Tunnel Research Methods Using the NASA Langley 12-Foot Low Speed Tunnel," *14th AIAA Aviation Technology, Integration, and Operations Conference*, AIAA Paper 2014-3000, Jun. 2014. https://doi.org/10.2514/6.2014-3000.

[22] Murphy, P. C., and Landman, D., "Experiment Design for Complex VTOL Aircraft with Distributed Propulsion and Tilt Wing," *AIAA Atmospheric Flight Mechanics Conference*, AIAA Paper 2015-0017, Jan. 2015. https://doi.org/10.2514/6.2015-0017.

[23] McSwain, R. G., Glaab, L. J., and Theodore, C. R., "Greased Lightning (GL-10) Performance Flight Research – Flight Data Report," NASA TM–2017–219794, Nov. 2017.

[24] Fredericks, W. J., McSwain, R. G., Beaton, B. F., Klassman, D. W., and Theodore, C. R., "Greased Lightning (GL-10) Flight Testing Campaign," NASA TM–2017–219643, Jul. 2017.

[25] Busan, R. C., Murphy, P. C., Hatke, D. B., and Simmons, B. M., "Wind Tunnel Testing Techniques for a Tandem Tilt-Wing, Distributed Electric Propulsion VTOL Aircraft," *AIAA SciTech 2021 Forum*, AIAA Paper 2021-1189, Jan. 2021. https://doi.org/10.2514/6.2021-1189.

[26] Geuther, S. C., North, D. D., and Busan, R. C., "Investigation of a Tandem Tilt-wing VTOL Aircraft in the NASA Langley 12-Foot Low-Speed Tunnel," NASA TM–2020–5003178, Jun. 2020.

[27] Simmons, B. M., "System Identification for Propellers at High Incidence Angles," *Journal of Aircraft*, Vol. 58, No. 6, 2021, pp. 1336–1350. https://doi.org/10.2514/1.C036329.

[28] Simmons, B. M., and Murphy, P. C., "Aero-Propulsive Modeling for Tilt-Wing, Distributed Propulsion Aircraft Using Wind Tunnel Data," *Journal of Aircraft*, Vol. 59, No. 5, 2022, pp. 1162–1178. https://doi.org/10.2514/1.C036351.

[29] Simmons, B. M., Morelli, E. A., Busan, R. C., Hatke, D. B., and O'Neal, A. W., "Aero-Propulsive Modeling for eVTOL Aircraft Using Wind Tunnel Testing with Multisine Inputs," *AIAA AVIATION 2022 Forum*, AIAA Paper 2022-3603, 2022. https://doi.org/10.2514/6.2022-3603.

[30] Simmons, B. M., Ackerman, K. A., Asper, G. D., Gray, M. N., Snyder, S. M., Axten, R. M., Geuther, S. C., and Chan, R., "Subscale Tiltrotor eVTOL Aircraft Dynamic Modeling and Flight Control Software Development," *Vertical Flight Society's 81st Annual Forum & Technology Display*, May 2025. https://doi.org/10.4050/F-0081-2025-161.

[31] Young, P. C., and Willems, J., "An Approach to the Linear Multivariable Servomechanism Problem," *International Journal of Control*, Vol. 15, No. 5, 1972, pp. 961–979.

[32] "PX4 Autopilot User Guide," https://docs.px4.io/main/en/, Accessed 03 December 2025.

[33] "MathWorks Documentation," https://www.mathworks.com/help/, Accessed 08 May 2025.

[34] Morelli, E. A., "Flight Test Maneuvers for Efficient Aerodynamic Modeling," *Journal of Aircraft*, Vol. 49, No. 6, 2012, pp. 1857–1867. https://doi.org/10.2514/1.C031699.

[35] Grauer, J., and Boucher, M., "Identification of Aeroelastic Models for the X-56A Longitudinal Dynamics Using Multisine Inputs and Output Error in the Frequency Domain," *Aerospace*, Vol. 6, No. 2, 2019, p. 24. https://doi.org/10.3390/aerospace6020024.

[36] Grauer, J. A., and Boucher, M. J., "Aircraft System Identification from Multisine Inputs and Frequency Responses," *Journal of Guidance, Control, and Dynamics*, Vol. 43, No. 12, 2020, pp. 2391–2398. https://doi.org/10.2514/1.G005131.

[37] Grauer, J. A., and Boucher, M. J., "Real-Time Estimation of Bare-Airframe Frequency Responses from Closed-Loop Data and Multisine Inputs," *Journal of Guidance, Control, and Dynamics*, Vol. 43, No. 2, 2020, pp. 288–298. https://doi.org/10.2514/1.G004574.

[38] Grauer, J. A., and Boucher, M., "System Identification of Flexible Aircraft: Lessons Learned from the X-56A Phase 1 Flight Tests," *AIAA SciTech 2020 Forum*, AIAA Paper 2020-1017, Jan. 2020. https://doi.org/10.2514/6.2020-1017.

[39] Perry, A. T., Bretl, T., and Ansell, P. J., "System Identification of a Subscale Distributed Electric Propulsion Aircraft," *Journal of Aircraft*, Vol. 60, No. 3, 2023, pp. 702–715. https://doi.org/10.2514/1.C036616.

[40] Gremillion, G., and Humbert, J. S., "System Identification of a Quadrotor Micro Air Vehicle," *AIAA Atmospheric Flight Mechanics Conference*, AIAA Paper 2010-7644, Aug. 2010. https://doi.org/10.2514/6.2010-7644.

[41] Wei, W., Cohen, K., and Tischler, M. B., "System Identification and Controller Optimization of a Quadrotor UAV," *AHS 71st Annual Forum*, May 2015.

[42] Niermeyer, P., Raffler, T., and Holzapfel, F., "Open-Loop Quadrotor Flight Dynamics Identification in Frequency Domain via Closed-Loop Flight Testing," *AIAA Guidance, Navigation, and Control Conference*, AIAA Paper 2015-1539, Jan. 2015. https://doi.org/10.2514/6.2015-1539.

[43] Tobias, E. L., Sanders, F. C., and Tischler, M. B., "Full-Envelope Stitched Simulation Model of a Quadcopter Using STITCH," *AHS International 74th Annual Forum & Technology Display*, May 2018.

[44] Sun, S., de Visser, C. C., and Chu, Q., "Quadrotor Gray-Box Model Identification from High-Speed Flight Data," *Journal of Aircraft*, Vol. 56, No. 2, 2019, pp. 645–661. https://doi.org/10.2514/1.C035135.

[45] Gong, A., Sanders, F. C., Hess, R. A., and Tischler, M. B., "System Identification and Full Flight-Envelope Model Stitching of a Package-Delivery Octocopter," *AIAA SciTech 2019 Forum*, AIAA Paper 2019-1076, Jan. 2019. https://doi.org/10.2514/6.2019-1076.

[46] Cho, S. H., Bhandari, S., Sanders, F. C., Cheung, K. K., and Tischler, M. B., "System Identification and Controller Optimization of Coaxial Quadrotor UAV in Hover," *AIAA SciTech 2019 Forum*, AIAA Paper 2019-1075, Jan. 2019. https://doi.org/10.2514/6.2019-1075.

[47] Kaputa, D. S., and Owens, K. J., "Quadrotor Drone System Identification via Model-Based Design and In-Flight Sine Wave Injections," *AIAA SciTech 2020 Forum*, AIAA Paper 2020-1238, Jan. 2020. https://doi.org/10.2514/6.2020-1238.

[48] Ivler, C. M., Rowe, E. S., Martin, J., Lopez, M. J., and Tischler, M. B., "System Identification Guidance for Multirotor Aircraft: Dynamic Scaling and Test Techniques," *Journal of the American Helicopter Society*, 2021. https://doi.org/10.4050/JAHS.66.022006.

[49] Leshikar, C., Eves, K., Ninan, N., and Valasek, J., "Asymmetric Quadrotor Modeling and State-Space System Identification," *2021 International Conference on Unmanned Aircraft Systems (ICUAS)*, IEEE, 2021, pp. 1422–1431. https://doi.org/10.1109/ICUAS51884.2021.9476871.

[50] Yuksek, B., Saldiran, E., Cetin, A., Yeniceri, R., and Inalhan, G., "System Identification and Model-Based Flight Control System Design for an Agile Maneuvering Quadrotor Platform," *AIAA SciTech 2020 Forum*, AIAA Paper 2020-1835, Jan. 2020. https://doi.org/10.2514/6.2020-1835.

[51] Niemiec, R., Ivler, C., Gandhi, F., and Sanders, F., "Multirotor Electric Aerial Vehicle Model Identification with Flight Data with Corrections to Physics-Based Models," *CEAS Aeronautical Journal*, Vol. 13, No. 3, 2022, pp. 575–596. https://doi.org/10.1007/s13272-022-00583-5.

[52] Alabsi, M. I., and Fields, T. D., "Real-Time Closed-Loop System Identification of a Quadcopter," *Journal of Aircraft*, Vol. 56, No. 1, 2019, pp. 324–335. https://doi.org/10.2514/1.C034219.

[53] Cunningham, M. A., and Hubbard, J. E., "Open-Loop Linear Model Identification of a Multirotor Vehicle with Active Feedback Control," *Journal of Aircraft*, Vol. 57, No. 6, 2020, pp. 1044–1061. https://doi.org/10.2514/1.C035834.

[54] Matt, J. J., and Altamirano, G. V., "System Identification of an Octocopter in Hover Using Full-Harmonic Orthogonal Multisine Inputs," *AIAA AVIATION Forum and ASCEND 2025*, AIAA Paper 2025-3886, Jul. 2025. https://doi.org/10.2514/6.2025-3886.

[55] Figueira, J. C., Bazzocchi, S., Warwick, S., and Suleman, A., "Nonlinear Aero-Propulsive Modeling for Fixed-Wing eVTOL UAV from Flight Test Data," *Journal of Aircraft*, Vol. 62, No. 2, 2025, pp. 300–312. https://doi.org/10.2514/1.C037964.

[56] Kunwar, B., Comer, A., Putra, S. H., Davis, B., McCormick, C., and Chakraborty, I., "Developing Flight Simulation Model for a Lift-Plus-Cruise Subscale Vehicle: Mass Properties, Propulsion, and System Identification," *AIAA SciTech 2025 Forum*, AIAA Paper 2025-0739, Jan. 2025. https://doi.org/10.2514/6.2025-0739.

[57] Simmons, B. M., Rapsomanikis, A., Jacobellis, G., Ofodile, N., Hamilton, T., and Ma, M., "Flight-Test System Identification Methodology and Hover Results for a Vectored-Thrust eVTOL Aircraft," *Vertical Flight Society's 81st Annual Forum & Technology Display*, May 2025. https://doi.org/10.4050/F-0081-2025-220.

[58] Simmons, B. M., and Busan, R. C., "Statistical Wind-Tunnel Experimentation Advancements for eVTOL Aircraft Aero-Propulsive Model Development," *AIAA SciTech 2024 Forum*, AIAA Paper 2024-2482, Jan. 2024. https://doi.org/10.2514/6.2024-2482.

[59] Simmons, B. M., "System Identification Approach for eVTOL Aircraft Demonstrated Using Simulated Flight Data," *Journal of Aircraft*, Vol. 60, No. 4, 2023, pp. 1078–1093. https://doi.org/10.2514/1.C036896.

[60] Simmons, B. M., Ackerman, K. A., and Asper, G. D., "Aeropropulsive Damping Characterization for eVTOL Aircraft Using Free Motion Wind-Tunnel Testing," *Journal of Aircraft*, Published Online 14 October 2025, pp. 1–15 (Article in Advance). https://doi.org/10.2514/1.C038339.

[61] "System IDentification Programs for AirCraft (SIDPAC)," *NASA Technology Transfer Program*, https://software.nasa.gov/software/LAR-16100-1, Accessed 08 May 2025.

[62] Morelli, E. A., "Multiple Input Design for Real-Time Parameter Estimation in the Frequency Domain," *13th IFAC Conference on System Identification*, Aug. 2003. https://doi.org/10.1016/S1474-6670(17)34833-4.

[63] Morelli, E. A., "Flight-Test Experiment Design for Characterizing Stability and Control of Hypersonic Vehicles," *Journal of Guidance, Control, and Dynamics*, Vol. 32, No. 3, 2009, pp. 949–959. https://doi.org/10.2514/1.37092.

[64] Morelli, E. A., "Practical Aspects of Multiple-Input Design for Aircraft System Identification Flight Tests," *AIAA AVIATION 2021 Forum*, AIAA Paper 2021-2795, Aug. 2021. https://doi.org/10.2514/6.2021-2795.

[65] Morelli, E. A., "Practical Aspects of the Equation-Error Method for Aircraft Parameter Estimation," *AIAA Atmospheric Flight Mechanics Conference and Exhibit*, AIAA Paper 2006-6144, Aug. 2006. https://doi.org/10.2514/6.2006-6144.

[66] Morelli, E. A., "Global Nonlinear Aerodynamic Modeling Using Multivariate Orthogonal Functions," *Journal of Aircraft*, Vol. 32, No. 2, 1995, pp. 270–277. https://doi.org/10.2514/3.46712.

[67] Klein, V., Batterson, J. G., and Murphy, P. C., "Determination of Airplane Model Structure from Flight Data by Using Modified Stepwise Regression," NASA TP-1916, Oct. 1981.

[68] Morelli, E. A., and Grauer, J. A., "Practical Aspects of Frequency-Domain Approaches for Aircraft System Identification," *Journal of Aircraft*, Vol. 57, No. 2, 2020, pp. 268–291. https://doi.org/10.2514/1.C035599.

[69] Morelli, E. A., “High Accuracy Evaluation of the Finite Fourier Transform Using Sampled Data,” NASA TM-110340, Jun. 1997.

[70] Young, H. D., *Statistical Treatment of Experimental Data*, McGraw-Hill, New York, 1962. Chapter 4.